Astron. Astrophys. 269, 541–563 (1993)

ASTRONOMY AND ASTROPHYSICS

The occultation of 28 Sgr by Titan

W.B. Hubbard[1], Bruno Sicardy[2], R. Miles[3], A.J. Hollis[4], R.W. Forrest[5], I.K.M. Nicolson[5], G. Appleby[6], W. Beisker[7], C. Bittner[7], H.-J. Bode[7], M. Bruns[7], H. Denzau[7], M. Nezel[7], E. Riedel[7], H. Struckmann[7], J.E. Arlot[8], F. Roques[2], F. Sèvre[9], W. Thuillot[8], M. Hoffmann[10,1], E.H. Geyer[10], C. Buil[11], F. Colas[8], J. Lecacheux[2], A. Klotz[11], E. Thouvenot[11], J.L.Vidal[12], E. Carreira[13], F. Rossi[13], C. Blanco[14], S. Cristaldi[14], Y. Nevo[15], H.J.Reitsema[16], N. Brosch[17], K. Cernis[18], K. Zdanavicius[18], L.H. Wasserman[19], D.M. Hunten[1], D. Gautier[2], E. Lellouch[2], R.V. Yelle[1], B. Rizk[1], F.M. Flasar[20], C.C. Porco[1], D. Toublanc[21],G. Corugedo[22]

[1] Lunar and Planetary Laboratory, University of Arizona, Tucson, Arizona 85721 USA
[2] Université Paris 6, Observatoire de Paris, F-92195 Meudon Cédex Principal, France
[3] Manley Observatory, Fernbank Farm, Sugar Lane, Manley, Cheshire WA6 9DZ, UK
[4] British Astronomical Association, Burlington House, Piccadilly, London WIV 9AG, UK
[5] University of Hertfordshire Observatory, Bayfordbury, Hertford, SG13 8LD, UK
[6] Royal Greenwich Observatory, Madingley Road, Cambridge CB3 0EZ, UK
[7] IOTA - European Section, Bartold-Knaust Straße 8, W-3000 Hannover 91, Germany
[8] Bureau des Longitudes, 77 Avenue Denfert-Rochereau, F-75014 Paris, France
[9] Institut d'Astrophysique de Paris, 98 Avenue Arago, F-75014 Paris, France
[10] Observatorium Hoher List der Universitätssternwarte Bonn, Germany
[11] Association du Télescope de 60 cm, Toulouse, France
[12] Observatoire du Pic du Midi et de Toulouse, F-65200 Bagnères de Bigorre, France
[13] Specola Vaticana, Vatican Observatory Research Group, I-00120 Cittá del Vaticano
[14] Istituto di Astronomia - Universitá di Catania, Viale Andre Doria, 6, I-95125 Catania, Italy
[15] Kibbutz Ein Harod, Meuchad 18965, Israel
[16] Ball Aerospace Systems Division, Boulder, Colorado 80306, USA
[17] Wise Observatory, Tel Aviv University, Ramat Aviv, Tel Aviv 69978, Israel
[18] Institute of Theoretical Physics and Astronomy, Gostauto 12, Vilnius 2600, Lithuania
[19] Lowell Observatory, Flagstaff, Arizona 86001, USA
[20] NASA Goddard Space Flight Center, Code 693, Greenbelt, Maryland 20771, USA
[21] Observatoire de Bordeaux, BP 89, F-33270 Floirac, France
[22] Applied Mathematics Program, University of Arizona, Tucson, Arizona 85721 USA

Received September 14, accepted October 12, 1992

Abstract. We present a comprehensive analysis of data obtained during the 1989 July 3 occultation of 28 Sgr by Titan. The data set includes 23 lightcurves from 15 separate stations, spanning wavelengths from 0.36 μm to 0.89 μm. A detailed model of the structure of Titan's atmosphere in the altitude range 250 to 450 km is developed, giving the distribution of temperature, pressure, haze optical depth, and zonal wind velocity as a function of altitude and latitude. Haze layers detected in Titan's stratosphere are about one scale height higher than inferred from *Voyager* data, and show a wavelength dependence indicative of particle sizes on the order of 0.1 μm. A marked north-south dichotomy in haze density is observed, with a transition to lower density south of about $-20°$ latitude. Zonal wind speeds are inferred from global distortions from spherical symmetry, and are of the order of 100 m/s, with significant increase toward higher latitudes. Titan's high atmosphere shows substantial axial symmetry; the position angle of the symmetry axis is equal to the position angle of Saturn's spin axis to within $\sim 1°$.

Key words: Titan – atmosphere – occultation

Send offprint requests to: W.B. Hubbard

1. Introduction

Saturn's largest satellite Titan occulted the bright K giant star 28 Sgr on 3 July 1989. Multiple observations provide very substantial fractional coverage of the occultation shadow, high time resolution and high signal/noise, and excellent range in wavelength. The center of the shadow passed over the most densely populated parts of Europe, providing numerous opportunities for coverage of the central caustics. This unusual event was observed by professional and amateur astronomers at stations in Europe, Central Asia, and the Middle East. The resulting

chords across Titan's shadow have impact parameters to the shadow center ranging from 200 km north of the center to more than 2000 km south of the center. Since the total radius of Titan's occultation shadow is nearly 3000 km (Sicardy et al. 1990; Hubbard et al. 1990), almost 50% of the shadow was covered with chords, at an averaged spacing of about 200 km. Our data set thus represent an enormous incomplete raster image of Titan's occultation shadow, with transverse and vertical dimensions of about 6000 km and 2500 km respectively. Although only about 15 fully independent raster lines are available in this image, the spatial resolution along an individual raster line (chord) is quite high, and equal to about 18 km, the projected diameter of 28 Sgr at Titan, (Hubbard et al. 1992), corresponding to about 1 s in time.

Owing to the large distance from the earth to Titan, $D = 1.35 \times 10^9$ km at the time of the occultation, the structure of the occultation shadow is determined by the integrated properties of Titan's atmosphere along the ray paths through the atmosphere, which can be well represented as straight lines with impact parameter $\mathbf{r}$ to the center of Titan. Titan's atmosphere can thus be represented for the purposes of this analysis by its integrated properties projected onto the reference plane, defined as a plane passing through the center of Titan and normal to the line connecting the center of Titan with the occulted star. Thus $\mathbf{r}$ is a two-component vector lying in the reference plane, with origin at the center of Titan. In this discussion, we express its components as x and y, which increase in the directions of celestial east and north respectively.

After suffering a small net bending angle α in Titan's atmosphere, a ray from the star to the observer eventually reaches a point with impact parameter $\mathbf{r}'$ to the center of curvature of the shadow. This point lies in the shadow plane, which passes through the center of the earth and is normal to the line connecting the center of Titan with the occulted star (Fig. 1). For all practical purposes, the angle α never exceeds the value (6000 km/D) = 4×10^{-6} radians. Thus the previously-stated assumption, that the rays are straight lines during propagation over a distance of $\sim$ 500 km through Titan's atmosphere, is an excellent one.

The occultation data set consists of measurements of $\phi(\mathbf{r}')$, where ϕ is the stellar flux in units of its unocculted value, and $\mathbf{r}'$ is a two-dimensional vector giving the observer's projected position on the shadow plane with respect to the center of the shadow pattern (Fig. 1). Clearly $\mathbf{r}'$ is parallel to $\mathbf{r}$. It has corresponding components x' (toward celestial east) and y' (toward celestial north). Our problem is to employ $\phi(\mathbf{r}')$ to determine the integrated properties of Titan's atmosphere as a function of $\mathbf{r}$, and then to deconvolve the results to determine the full three-dimensional structure of the atmosphere.

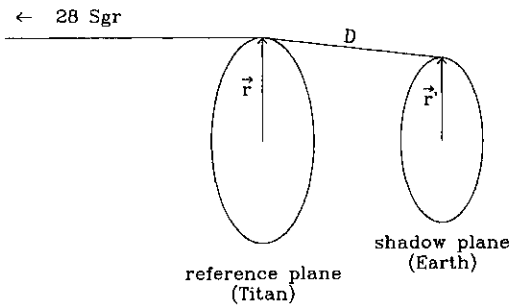

Fig. 1. Definition of reference plane and shadow plane

The region of Titan's atmosphere which is probed by this data set extends over altitudes h from about 250 km to about 500 km above Titan's surface, a region which was not extensively investigated by the Voyager spacecraft. The spacecraft experiments obtained detailed atmospheric profiles in the altitude range h = 0 to 200 km (radio-occultation; Lindal et al. 1983), and $h > 1000$ km (UV occultation; Smith et al. 1982). Considerations of hydrostatic equilibrium constrain the average temperature profile in the intermediate altitude range corresponding to the spacecraft data gap. Model temperature profiles have been calculated in the gap range $200 < h < 1000$ km (Lellouch et al. 1990; Yelle 1991) using this constraint, and can in principle be tested by our data set. An investigation of particulate hazes in Titan's atmosphere using Voyager images (Rages & Pollack 1983; hereafter RP) provides a prediction of vertical and tangential optical depths as a function of h, which can also be tested by the occultation data. Using the RP haze model in combination with any of the model atmospheres which cover the gap range, we would predict essentially negligible tangential optical depth for photons reaching any point in the occultation shadow. However, the strong evidence for wavelength-dependent occultation profiles near the center of the shadow (Sicardy et al. 1990; Hubbard et al. 1990) shows that the RP model was not a valid representation of Titan's atmosphere on 3 July 1989.

Our paper is organized as follows. Station parameters and descriptions of individual experiments are briefly summarized in Sect. (2). In Sect. (3) we calculate shadow profiles for a loss-free Titan atmosphere, and compare them with the observations. This establishes the regions of the atmosphere which can be considered to be loss-free (i.e., the tangential optical depth τ can be considered negligible). We then carry out a formal inversion of the loss-free portions of the lightcurves to obtain the background temperature profiles. In Sect. (4) we analyze the portions of the lightcurves where τ appears to be important, and use the results to infer properties of the Titan hazes. In Sect. (5) we discuss the region of the shadow where the mapping $\mathbf{r}' \rightarrow \mathbf{r}$ becomes singular, i.e., the "central flash".

The volume and quality of the data and the complexity and interrelatedness of the various processes which give rise to the complete occultation shadow pose a particularly daunting problem in modelling. Thus, although we present the separate aspects of the modelling in a linear fashion, it must be recognized that each aspect has a nonnegligible impact on every other aspect, and the proper way to read this paper is in the same way that the analysis was performed, i.e. in a recursive fashion. Our overall philosophy has been to strive for economy of parameters, to seek the simplest model to account for features in the data which repeat at two or more stations and which therefore seem to be globally significant. Nevertheless, the model is not simple, and the number of parameters is such that a formal error analysis is not feasible. Indeed, computation of a full set of

model lightcurves for all stations and wavelengths requires several minutes of CPU time on the latest Sun 4/370 workstation. Derivation of a fully-optimized model in a least-squares sense would require on the order of one year of CPU time. Thus, the preferred model has been obtained by sequential and recursive partial optimization of a subset of the parameters. Parameters of the preferred model are presented with estimated uncertainties.

2. Summary of individual experiments

In this paper we present an analysis of all data that we were able to obtain in digital form with sufficient signal/noise and signal stability to admit quantitative comparison with model lightcurves.

Table 1 lists the geographically separate stations contributing data to this paper, as well as multiple individual experiments at each station. Many of the experiments have been described in more detail in other publications (Beisker et al. 1989; Sicardy et al. 1990; Hubbard et al. 1990; Forrest & Nicolson 1990) Table 2 lists the personnel at each observing site.

Figure 2 shows all chords for stations with photometric data, projected on the $\mathbf{r}'$ plane. These chords were derived from an ephemeris calculated by L.H. Wasserman for Titan, predicting apparent geocentric positions at 6, 12, 18 hrs ET on 3 July 1989, and at 0, 6 hrs ET on 4 July 1989. The apparent stellar positions at the same times were then calculated, and corrections for station offsets from the geocenter applied. Finally, the relative offset of star from Titan in the reference plane was adjusted for best fit of the lightcurves to the data. That is, if the ephemeris position of a station at time t is given by x'_E, y'_E on the $\mathbf{r}'$ plane, we subtract from the coordinates of each station a constant offset x'_0, y'_0, such that $x' = x'_E - x'_0$ and $y' = y'_E - y'_0$.

We performed the following steps to reduce the individual data sets to similar form for comparison with models. First, data taken at rates substantially higher than 1 hz were smoothed to a time resolution of approximately 1 s, about the time required to

Table 2. Observers

Location	Personnel
Manley Obs., UK	R. Miles, A.J. Hollis
Hertford Obs., UK	R.W. Forrest, I.K.M. Nicolson
Royal Greenwich Obs., UK	G. Appleby
Heikendorf, Germany	E. Riedel
Langwedel, Germany	M. Nezel, M. Bruns, H. Struckmann
Essen, Germany	H. Denzau
Hannover, Germany	H.-J. Bode, C. Bittner
Meudon Obs., France	J.E. Arlot, F. Roques, F. Sèvre, W. Thuillot
Hoher List Obs., Germany	M. Hoffmann, E.H. Geyer
Pic du Midi Obs., France	J. Lecacheux, B. Sicardy, C. Buil, F. Colas, A. Klotz, E. Thouvenot, J.L. Vidal
Vatican Obs., Italy	E. Carreira, F. Rossi
Catania Obs., Italy	C. Blanco, S. Cristaldi
Ein Harod, Israel	H.J. Reitsema, Y. Nevo
Wise Obs., Israel	N. Brosch
Maidanak Obs., Uzbekistan	K. Zdanavicius, K. Cernis

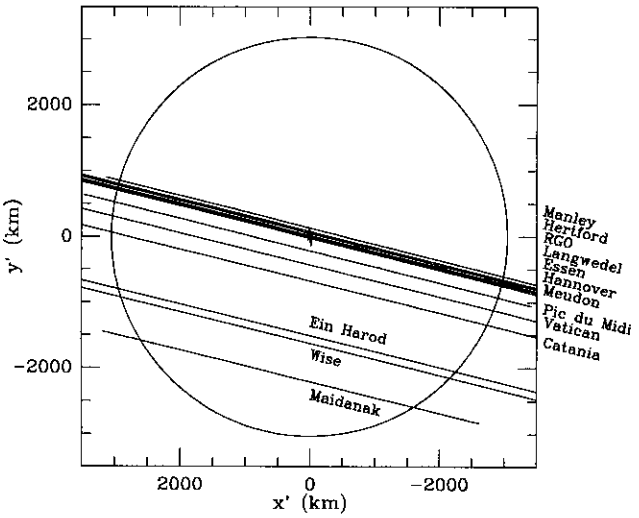

Fig. 2. Tracks (chords) of stations across the shadow plane. The circular outline shows the half-flux locus. The spindle-shaped outline near the center shows the location of central caustics (shown in more detail in Fig. 33)

Table 1. Stations and individual experiments

Location	Telescope	λ (μm)	Sampling (hz)	Latitude	Longitude	Elev. (m)
Manley Obs., UK	0.35/0.28 m	0.55	5	53° 14' 43"	2° 44' 15" W	75
Hertford Obs., UK	0.36 m	0.72	10	51° 46' 28"	0° 5' 31" W	66
Royal Greenwich Obs., UK	0.5 m	0.532	5	50° 52' 10"	0° 20' 51" E	50
Heikendorf, Germany	0.15 m	0.55	5	54° 20' 33"	10° 4' 44" E	10
Langwedel, Germany	0.3 m	0.55	5	52° 58' 37"	9° 11' 3" E	20
Essen, Germany	0.36 m	0.55	5	51° 24' 35"	7° 4' 15" E	94
Hannover, Germany	0.4 m	0.45 to 0.85	5	52° 21' 25"	9° 44' 55" E	80
Meudon Obs., France	0.6 m	0.44	18.2	48° 48' 18"	2° 13' 53" E	100
Meudon Obs., France	1 m	0.45 to 0.85	4.7	48° 48' 18"	2° 13' 53" E	100
Hoher List Obs., Germany	1.06 m	0.55	5	50° 9' 45"	6° 51' 0" E	533
Pic du Midi Obs., France	1 m	0.44	1.8	42° 56' 12"	0° 8' 32" E	2861
Pic du Midi Obs., France	0.6 m	0.65	0.58	42° 56' 12"	0° 8' 32" E	2861
Pic du Midi Obs., France	2 m	0.75/0.89	20	42° 56' 12"	0° 8' 32" E	2861
Vatican Obs., Italy	0.61 m	0.45/0.8	100	41° 44' 48"	12° 39' 6" E	450
Catania Obs., Italy	0.61 m	0.36/0.44/0.55	0.71	37° 41' 30"	14° 58' 42" E	1725
Catania Obs., Italy	0.91 m	0.44	1	37° 41' 30"	14° 58' 42" E	1725
Ein Harod, Israel	0.36 m	0.45/0.8	100	32° 33' 35"	35° 23' 42" E	20
Wise Obs., Israel	1 m	0.73	20	30° 35' 48"	34° 45' 48" E	900
Maidanak Obs., Uzbekistan	1 m	0.544	0.33	38° 41' 3"	66° 54' 30" E	2540

sweep through one stellar diameter. Second, lightcurves were normalized to a mean value of unity outside of occultation, and to a mean value of zero when only the signal from Titan and the sky background alone was present. The zero level was obtained from calibration observations at each site where these were available. In many cases, a reliable zero level was not available, or was strongly inconsistent with plausible theoretical lightcurves. In these cases a constant zero level was inferred by other means. For example, zero levels were calibrated at Ein Harod and Wise Observatory, but not at Vatican Observatory (where clouds were present during the initial seconds of the occultation). But since identical photometers were used at Ein Harod and Vatican, the stellar scintillations in Titan's atmosphere near midoccultation could be used to normalize the flux at Vatican. That is, we assumed that the rms scintillation amplitude was proportional to the mean stellar flux over some appropriate averaging interval, and the proportionality constant inferred from the Ein Harod and Wise data was used to renormalize the Vatican data. The best-fit atmospheric models with realistic haze optical depths (see below) show that the normalized stellar flux observed at stations near the center of the shadow should at times be essentially zero. Thus, for such stations the zero level was adjusted for consistency with the model, usually by setting zero at the minimum signal level.

3. Lightcurves and inversions for a loss-free atmosphere

A general theory for calculating the lightcurve $\phi(\mathbf{r}')$ for a spherical planet with a weakly bound atmosphere and an arbitrary variation of temperature T with height h is presented by Hubbard, Yelle, & Lunine (hereafter HYL, 1990). Here h is the height of a point in the atmosphere above the solid surface of Titan at a radius of 2575 km. A weakly bound atmosphere is one where the gas scale height H (approximately 50 km for Titan) is sufficiently large compared with the atmospheric radius a (about 3000 km) that all terms in H/a must be retained. The HYL theory is a generalization of the theory for a weakly bound isothermal atmosphere presented by Hubbard et al. (1988a). HYL also present a general solution to the inverse problem, that is, determination of the profile of gas refractivity $N(h)$ from a knowledge of $\phi(\mathbf{r}')$. Once $N(h)$ is determined, we integrate the equation of hydrostatic equilibrium

$$\frac{1}{T}\frac{dT}{dh} + \frac{g\mu}{RT} = -\frac{1}{N}\frac{dN}{dh}, \tag{1}$$

where g is the local gravity, R is the ideal gas constant, $\mu = 28$ amu is the mean molecular weight (assuming pure nitrogen gas), and it is assumed that N is proportional to the gas mass density ρ, as discussed below. Equation (1) is integrated from a starting temperature at high altitude h, obtained from a model atmosphere constrained by Voyager data, as described below. Once $T(h)$ becomes available from the solution to Eq. (1), the gas pressure P is obtained from the equation of state $P = R\rho T/\mu$.

The dependence of refractivity N on wavelength λ plays only a minor role in the determination of atmospheric structure. Because $N(\lambda)$ is a decreasing function of λ, at a given point in the lightcurve the bending angle α is smaller at longer wavelengths, and therefore at longer wavelengths the stellar flux probes slightly deeper in Titan's atmosphere. In this paper we assume the following dispersion formula for nitrogen gas:

$$\frac{3}{2}\frac{N_{STP}^2 - 1}{N_{STP}^2 + 2} \times 10^6 = \frac{\beta'}{\mu' - \lambda^{-2}} + \frac{\beta''}{\mu'' - \lambda^{-2}}, \tag{2}$$

where $\beta' = 39534$, $\beta'' = -8373.4$, $\mu' = 152.294$, $\mu'' = -240.651$, λ is in μm, and N_{STP} denotes the refractivity at standard temperature and pressure (Washburn 1930). To scale from N_{STP} to N at mass density ρ, we multiply N_{STP} by the factor $\rho/(28L$ amu), where L is Loschmidt's number and amu is the atomic mass unit. Using Eq. (2), we find that the maximum difference in h between the projected stellar images at the shortest wavelength of observation (0.36 μm) and the longest wavelength (0.89 μm) at the greatest bending angle (near the center of the shadow) is only about 2 km, or about 0.1 stellar diameter.

Several assumptions play an essential role in the inversion procedure. First, it is assumed that photons are conserved as they propagate through the occulting atmosphere. Thus the density of photons received per unit area at the earth is modified only by differential refraction, which permits the functional dependence $\phi(\mathbf{r}')$ to be analyzed to obtain the distribution of net refractive bending angles α (where $D\alpha(h) = |\mathbf{r} - \mathbf{r}'|$). Second, it is assumed that photons are refracted in a plane containing the observer and the projected gradient of the mean occulting atmosphere. If atmospheric turbulence is present, its effect in scattering photons out of this plane is assumed to be zero on average. Third, it is assumed that detectable flux is obtained from only one stellar image at a time. If significant flux is received from more than one stellar image, as can in principle occur in a weakly-bound, loss-free planetary atmosphere, it is necessary to know the separate contributions of each image to $\phi(\mathbf{r}')$ in order to obtain the distribution of bending angles. Such information can in principle be obtained from area detectors with sufficient resolution, but was not in general available for the Titan data.

The first step in the inversion process is to establish the portions of the shadow which can be considered loss-free. Since models of the relevant altitude range (Lellouch et al. 1990; Yelle 1991) show that temperature gradients are not sufficiently large to strongly affect the lightcurves, we may assume an isothermal atmosphere to first approximation. The assumed mean temperature ranges from a minimum of 151 K (Yelle model a) to a maximum of 174 K (Lellouch et al. 1990). Figure 3 shows data from several of the chords, illustrating various degrees of sensitivity to hazes in the deeper levels of Titan's stratosphere. The theoretical curves are calculated using a temperature $T = 174$ K, and a projected atmospheric oblateness of 0.015 (see below). They are fitted to the outer edges of the shadow by adjusting the offset of the ephemeris position of Titan with respect to the star, but a fit to the center of the shadow is obviously impossible without drastic changes to the assumed model. While a strong temperature inversion at the bottom of the probed region can lead to a strong suppression of the flux in a loss-free at-

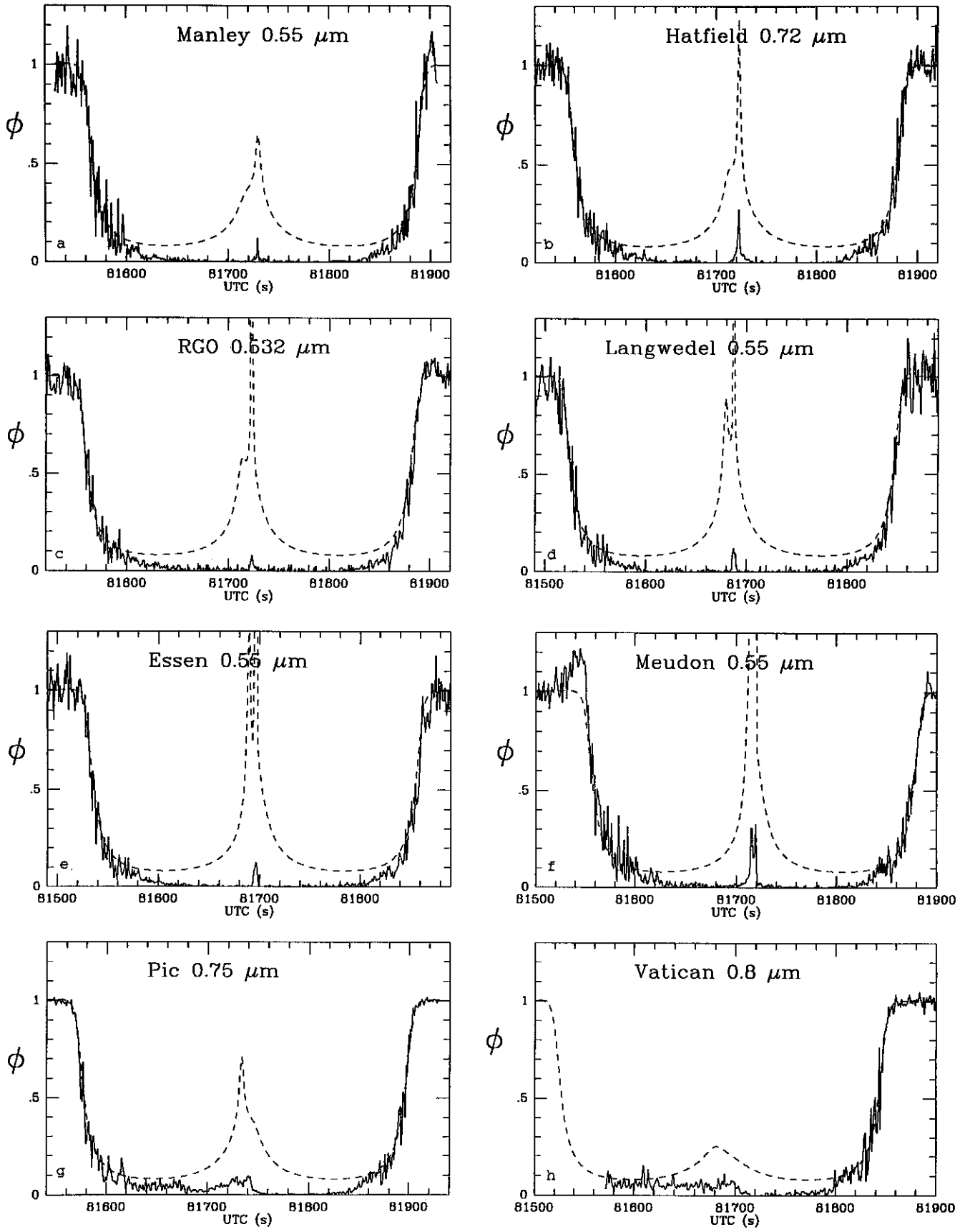

Fig. 3. Comparison of data (solid curves) and theory with zero haze optical depth (dashed curves) for several lightcurves. Note the substantial loss of signal at the bottom of the observed lightcurves

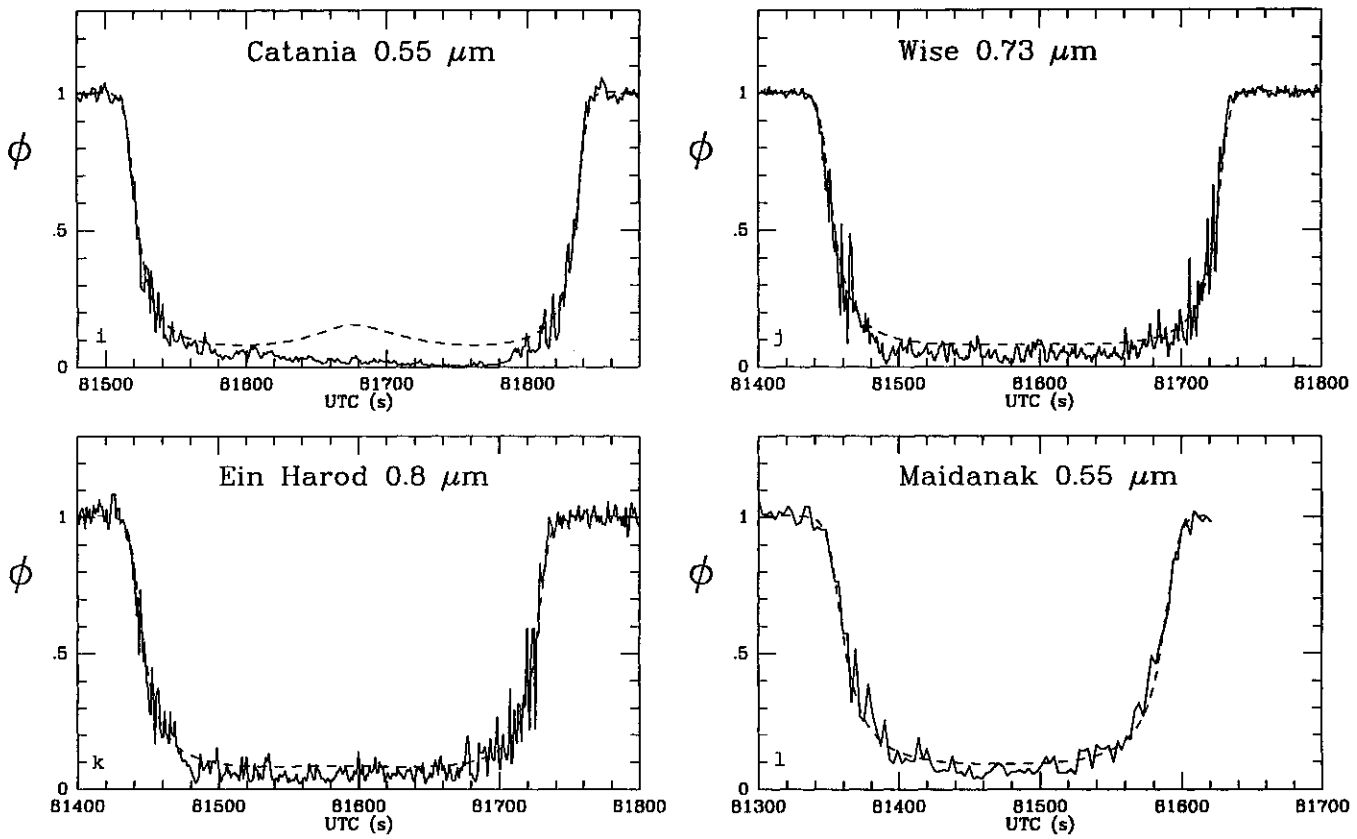

Fig. 3. (continued)

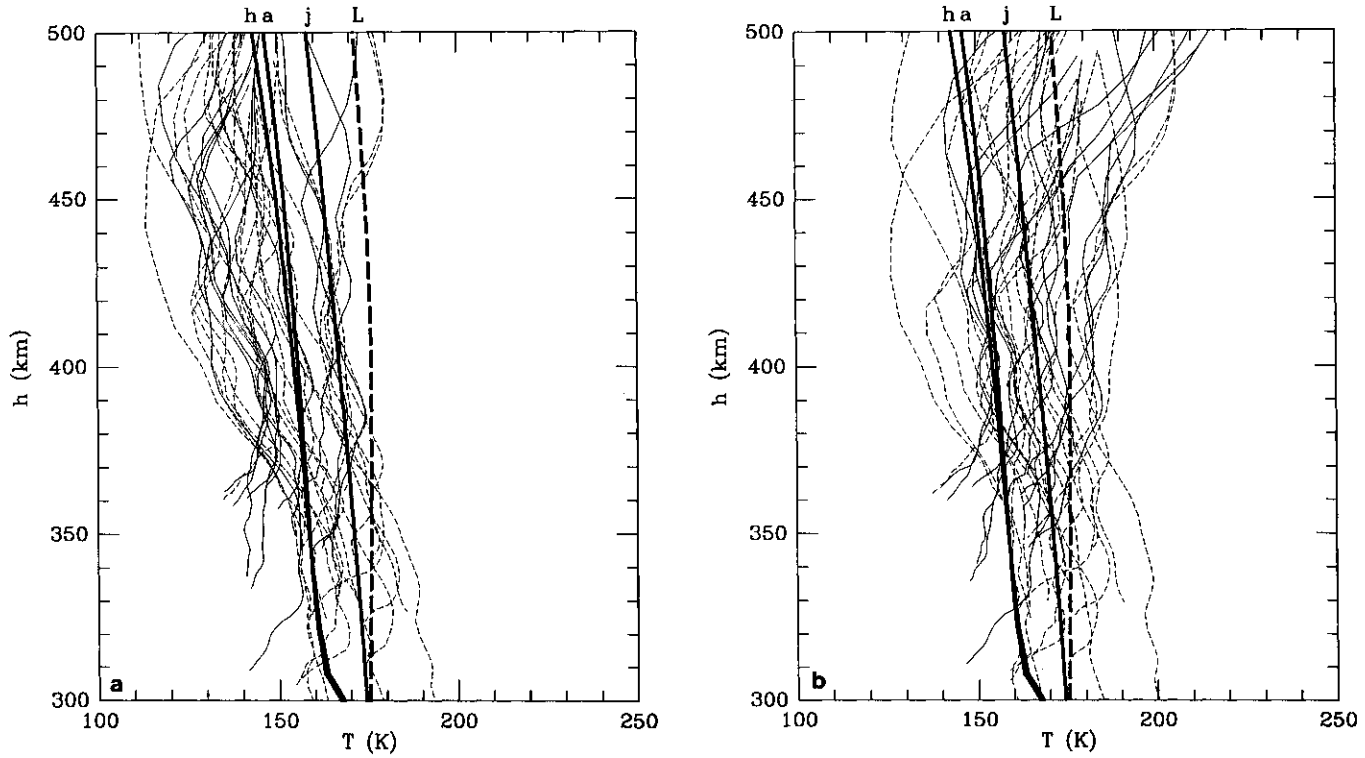

Fig. 4. Comparison of model atmospheres (heavy curves) and inversions for temperature vs. altitude above Titan's solid surface at r = 2575 km (lighter curves), assuming a loss-free atmosphere with no horizontal scattering. The solid curves are from chords which primarily sampled the northern hemisphere of Titan, while dashed curves are from chords which primarily sampled the southern hemisphere. (a) Inversions started from Yelle model *a* at high altitude; (b) inversions started from the Lellouch model

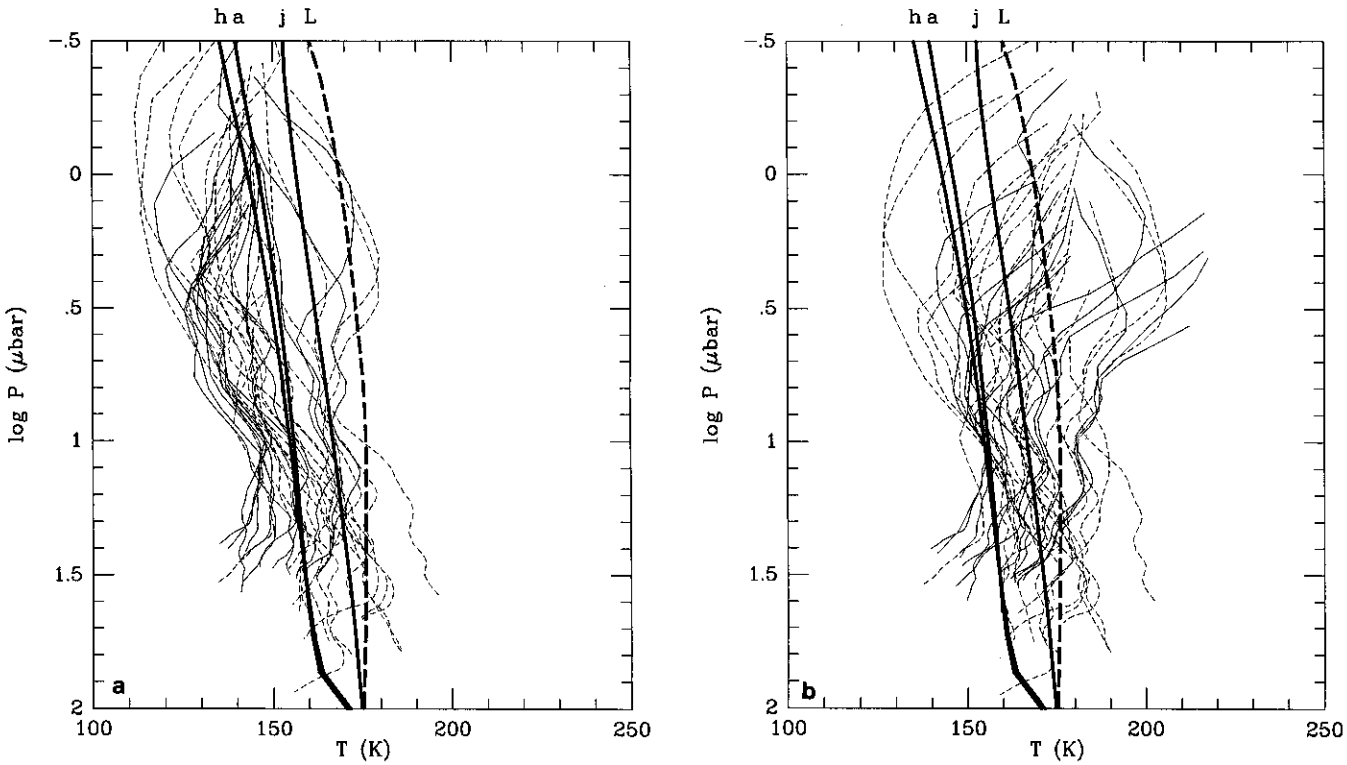

Fig. 5. Same as Fig. 4, but for temperature vs. pressure

mosphere (Eshleman 1989; HYL), such an inversion is highly implausible in Titan's atmosphere in the 250-300 km altitude range. Moreover, a temperature inversion would lead to essentially wavelength-independent flux suppression, while the data show strong wavelength dependence (see, e.g., Figs. 15-18, below).

With the results of Fig. 3 as a guide, we then conducted an inversion of each lightcurve using the method of HYL, terminating the inversion at the level where the best-fit haze model (see below) predicted a tangential optical depth τ in excess of 0.2. The haze model shows that we are always justified in neglecting the far-limb image when inverting the flux where $\tau < 0.2$ for the near-limb image.

Results of the inversions are summarized in Fig. 4 (a,b) and Fig. 5 (a,b). These plots show individual lightcurve inversions (lighter curves) compared with models. The models marked h, a, and j are from Yelle (1991), using his nomenclature, while the model marked L is from Lellouch et al. (1990). As is well known, inversions are sensitive to the initial temperature value adopted at the high-altitude starting point. The effect of this sensitivity is shown in version (a) and (b) of each figure, where the inversions are respectively started from Yelle model a and from the Lellouch model at high altitude. The scatter between the individual inversions appears to be the result of noise in the zero-point value (at low altitudes), and noise in the starting value for the bending angle (at high altitude), thus the ensemble of inversions demonstrates the range of uncertainty in an individual inversion rather than real variations from point to point in Titan's atmosphere.

We have coded the inversions in various ways, seeking systematic variations with wavelength, and with immersion vs. emersion. The only station-to-station variation which is evident is the north-south variation, which appears in the sense that the inversions from northern chords show a pronounced downturn in temperature with decreasing altitude (increasing pressure) at altitudes $h < 380$ km. This effect is not caused by a real decrease in temperature, but rather reflects the onset of a drop in stellar flux caused by rapidly-increasing haze optical depths in the northern chords.

We conclude from the inversions for temperature that (a) mean temperatures in Titan's stratosphere lie in the range 150-170 K, and are probably slightly cooler than values given by the Lellouch model, and slightly warmer than values given by the coldest Yelle models; (b) there is no evidence for significant temperature differences between the sunset (immersion) limb and sunrise (emersion) limb, or for differences between the northernmost (equatorial) and southernmost (high southern latitudes) chords.

4. Titan's stratospheric hazes

RP carried out the first detailed analysis of vertical haze optical depths in Titan's atmosphere, based on *Voyager 2* images of the atmosphere. Utilizing the leftmost panel of Fig. 4 from RP, and assuming that the equatorial profile pertains to the entire atmosphere, we infer a vertical optical depth $\tau_v = 0.1$ at an altitude $h = 225$ km. The scale height for the vertical haze optical

depth H_τ inferred from RP's analysis is $H_\tau \sim 30$ km; thus the tangential optical depth τ is given by

$$\tau = 0.1 \times \sqrt{2\pi r/H_\tau}\, \exp[(225 - h)/H_\tau], \quad (3)$$

where r and h are expressed in km, $r = 2575 + h$, and the value of τ applies to visual wavelengths.

Equation (3) does not predict significant haze optical depths at any of the altitudes probed by the stellar occultation observations. The minimum altitude probed by the occultation depends on the stratospheric temperature, in the sense that the higher the temperature, the smaller (deeper) the minimum altitude at deepest penetration. For a mean stratospheric temperature $T = 174$ K, the minimum altitude is 257 km, while for $T = 151$ K it increases to 285 km. However, even with the warmest model at $T = 174$ K, Eq. (3) fails to provide sufficiently large values of τ to agree with the data.

It is also evident from the data that a single $\tau(h)$ relationship fails to describe the lightcurves for the chords north of Ein Harod, which probe a substantial range of latitudes on Titan. Were there a single such relationship, any asymmetry between the immersion and emersion parts of the lightcurves would be due only to deviations of Titan's atmosphere from a spherical shape. Some stations, such as Pic du Midi, Vatican, and Catania, show pronounced asymmetries which cannot be ascribed to departures from sphericity. Detailed comparison of the stellar flux with the calculated position of the main stellar image as a function of time at each of these stations shows that the flux tends to change rapidly with time when the image has reached a critical angular distance from the projected spin axis of Titan, assuming that the latter is collinear with Saturn's spin axis. That is, the data from Pic du Midi, Vatican, and Catania indicate that there are two haze regimes in Titan's stratosphere: a haze regime of relatively low optical depth which extends over Titan's south pole, and a regime of relatively high optical depth which extends over the north pole and equatorial regions. A transition between the haze regimes appears most noticeably in the Pic du Midi data at about 81750 UTC, and in the Vatican data at about 81700 UTC. The regimes appear to be symmetric about Titan's spin axis. Further confirmation of the two-haze model emerges from its partial successes in accounting for asymmetries in central flashes at stations north of Pic du Midi.

4.1. A Titan haze model

We assume that there are two haze components in Titan's stratosphere: a high-altitude haze, and a component at lower altitudes. The lower-altitude haze is assumed to be present everywhere, while the high-altitude haze is restricted to only certain Titan latitudes. Thus we parameterize Titan's stratospheric haze with six parameters: τ_{0L}, τ_{0H}, $H_{\tau L}$, $H_{\tau H}$, q, and $\tilde{\theta}_c$. These parameters are respectively: (a) the tangential optical depth at a reference altitude (arbitrarily chosen equal to 318 km) and reference wavelength (arbitrarily chosen equal to 0.50 μm), for the low haze component; (b) the same quantitity for the high haze component; (c) the scale height of the low haze component; (d) the same quantity for the high haze component; (e) the index for the wavelength dependence of the optical depth, assumed to be independent of altitude and the same for the two haze components. Finally, we define $\tilde{\theta}$ to be the angle from the projected north pole of Titan in the reference plane to the ray closest approach point $\mathbf{r}$, so that $\tilde{\theta}$ is given by $\mathbf{r} \cdot \mathbf{e}_N = r \cos\tilde{\theta}$, where $\mathbf{e}_N$ is a unit vector collinear with Titan's spin axis projected in the reference plane. Thus (f) we define $\tilde{\theta}_c$ such that if $\tilde{\theta} < \tilde{\theta}_c$, both haze components are present. When $\tilde{\theta} \geq \tilde{\theta}_c$, only the low haze is present. The tangential optical depth is then given by

$$\tau = \tau_{0L}\left(\frac{0.5}{\lambda}\right)^q \exp\left[\frac{318 - h}{H_{\tau L}}\right] \quad (4)$$

for $\tilde{\theta} \geq \tilde{\theta}_c$, and

$$\tau = \tau_{0L}\left(\frac{0.5}{\lambda}\right)^q \exp\left[\frac{318 - h}{H_{\tau L}}\right] + \tau_{0H}\left(\frac{0.5}{\lambda}\right)^q \exp\left[\frac{318 - h}{H_{\tau H}}\right] \quad (5)$$

for $\tilde{\theta} < \tilde{\theta}_c$, where h is in km and λ is in μm.

The haze parameters were adjusted by least-squares to obtain a best fit to the ensemble of lightcurves. The resulting values are presented in Table 3. As has been explained, the values are correlated with the assumed stratospheric temperature profile. Error bars are estimated.

Our Titan haze model is compared with the RP model in Fig. 6. The principal differences with RP are (a) we find the hazes to be approximately one pressure scale height higher in the atmosphere, and (b) we find the haze scale heights to be a factor of two to three smaller than the value deduced by RP. Since

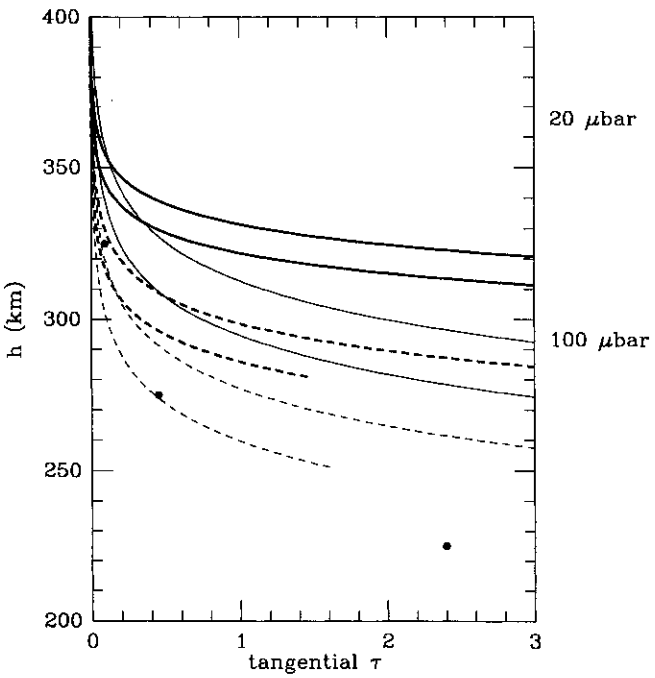

Fig. 6. Optical depth of Titan hazes vs. altitude. *Dots* show the RP model. *Heavy curves* are the occultation model for Yelle model atmosphere *a*; *light curves* are for the Lellouch model atmosphere. *Dashed curves* are for the low optical depth regime in Titan's southern hemisphere; *solid curves* are for the high optical depth regime for $\tilde{\theta} < \tilde{\theta}_c$. Each pair of curves shows $\tau(h)$ for $\lambda = 0.45$ μm (upper) and $\lambda = 0.8$ μm (lower)

Table 3. Parameters for Titan haze model from 28 Sgr occultation data

model atmosphere	τ_{0L}	τ_{0H}	H_{rL} (km)	H_{rH} (km)	q	$\tilde{\theta}_c$ (deg)
Lellouch (174 K)	0.084	0.628	18	18	1.7 ± 0.2	117 ± 1
Yelle *a* (151 K)	0.183	3.35	12.7	9.7	1.7 ± 0.2	117 ± 1

the denser haze layer is found in Titan's summer hemisphere in 1989, the structure of the hazes may well be governed by solar photons, and thus be substantially time-dependent.

Extrapolation of our haze model to lower altitudes than those probed by the occultation yields unrealistically large vertical optical depths, which may be in conflict with sufficient atmospheric transparency to allow formation of infrared gas absorption features. Resolution of this discrepancy may lie in the recognition that the haze seen in the stellar occultation corresponds to the high detached haze layer seen in *Voyager* images. Although it reaches large tangential optical depths, it may terminate before its vertical optical depth becomes substantial.

4.2. *Image positions in the reference plane*

The relatively simple haze distribution model transforms into complex effects on the lightcurves because of a combination of the nonuniform motion of the stellar image in the reference plane, as seen from each station, together with the orientation of the Titan globe with respect to the chords. Figure 7(a,b,c,d)

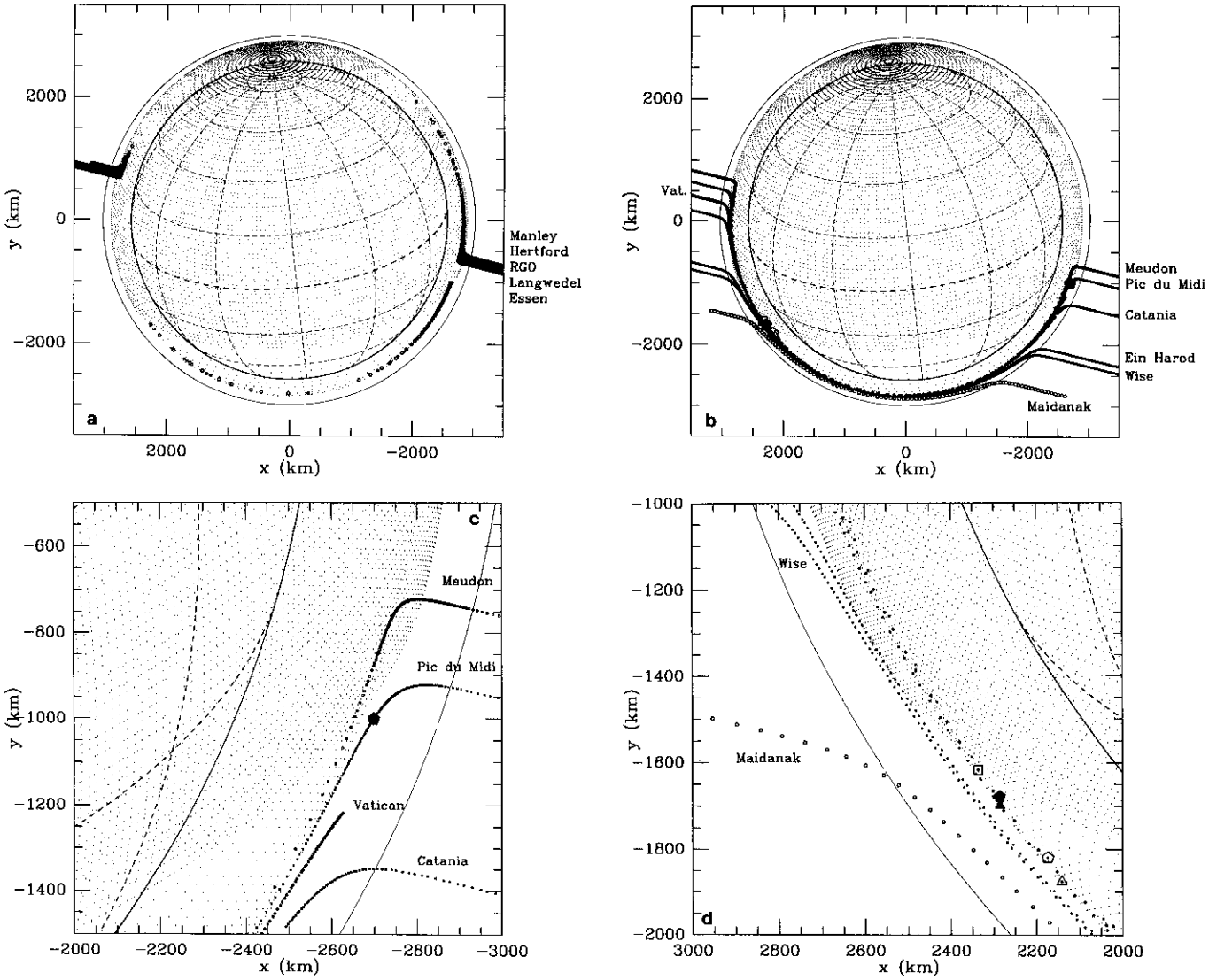

Fig. 7. Locations of stellar images in the reference plane, as a function of time, for various stations. Positions are calculated for a nonspherical atmosphere (see following section), and for an isothermal atmosphere. Differences in position for an atmosphere at T = 174 K and for T = 151 are indistinguishable at these scales

shows the location of the brightest image seen from each station as a function of time, plotted on the reference plane. For clarity, images for northern stations are plotted in Fig. 7a, for southern stations in Fig. 7b, and enlargements of the part of the limb where the stellar image enters or leaves the low optical depth regime are shown in Figs. 7c and 7d. The outermost (light line) circle shows the locus with an equatorial radius at r = 3031 km where the first modulation of the stellar signal by atmospheric refraction is observed. The innermost heavy circle shows the solid surface of Titan at r = 2575 km. Shading denotes the denser northern haze layer, which abruptly gives way to the less-dense southern haze at a Titan latitude of $-20°$. The image locations are generally plotted at a time interval of approximately 1 s, except for Maidanak, where the interval is 3 s. Large symbols denote times where significant signal level changes occur, indicative of entry or exit from a haze layer (see also the lightcurves plotted in Figs. 8-26).

In Fig. 7, the images move from right (negative values of x) to left (positive values of x) as time increases. Note in Fig. 7a that the brightest images appear discontinuously in the relatively clear southern polar region during the times of mid-event. That is, when the observer is near a caustic, the brightest image, which would normally be in Titan's northern hemisphere for a northern observer, shifts abruptly to the south polar region, where the haze opacity is smaller.

4.3. Comparison of model lightcurves with data

The haze model presented in Eqs. (4) and (5) and Table 3 is able to fit the lightcurves quite well. In Figs. 8-26, we compare the data (solid curves) with a best-fit model (dashed curves). These lightcurves correspond to all of the experiments listed in Table 1, with the exception of the Meudon 0.6 m, and the Heikendorf and Hoher List stations. Data from the Meudon 0.6 m have insufficient signal/noise for analysis in this study (these data have been published by Sicardy et al. 1990); the Heikendorf and Hoher List data are presented and discussed in Sect. 5.5 below.

In Figs. 8-26, points on the lightcurves which correspond to entry or exit from a haze layer are marked with symbols as in Fig. 7(a,b,c,d). The models plotted in Figs. 8-26 are computed using the Yelle a model atmosphere and corresponding haze parameters; models computed using the Lellouch parameters are virtually indistinguishable. In Figs. 8 and 9 only, we also plot theoretical central flash profiles for the best-fit simple oblate model (open circles).

The asymmetric north-south haze distribution has two major effects on the lightcurves. Well away from the central caustic region, we see substantial suppression of flux on one side of midevent but not the other, as is particularly evident in the Pic du Midi, Vatican, and (to a lesser extent) Catania data. As Fig.

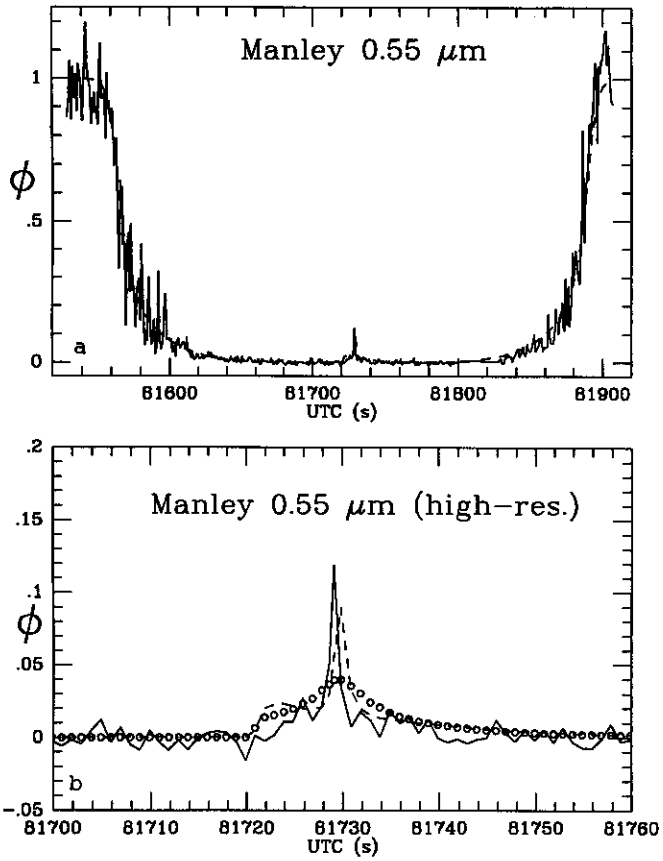

Fig. 8. (a) Data and model for Manley, the northernmost station. Note the pronounced central flash. (b) Comparison of data and model in the vicinity of the central flash. For a simple oblate atmosphere (open circles), the model gives a much smaller central flash

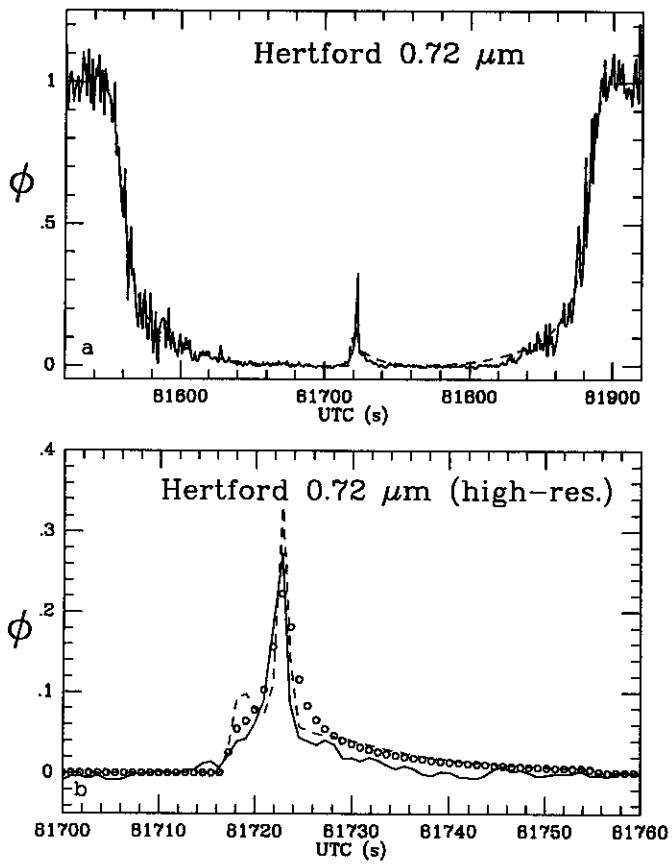

Fig. 9. Data and model for Hertford. The asymmetric central flash is produced by a combination of asymmetric haze opacity and a complex caustic pattern

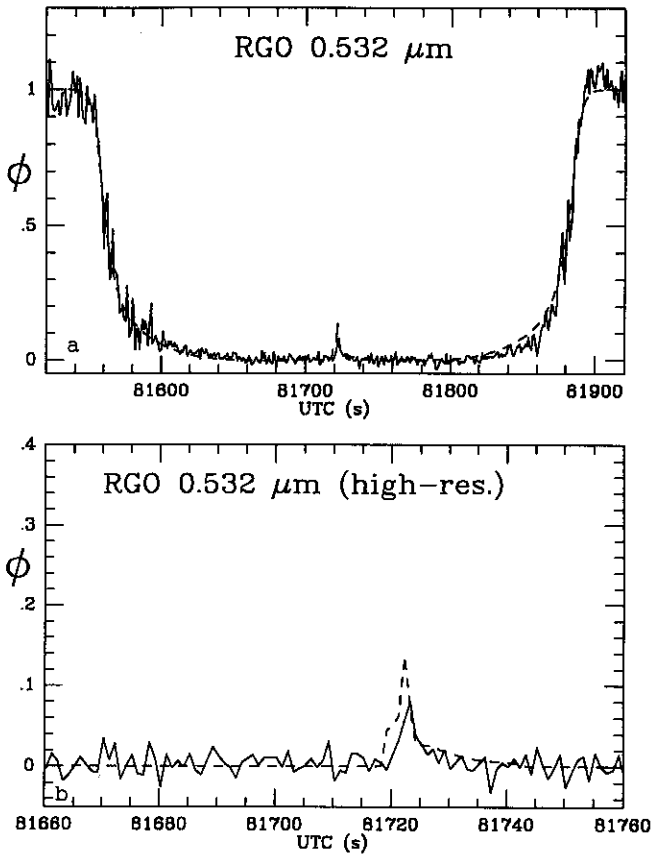

Fig. 10. Data and model for RGO

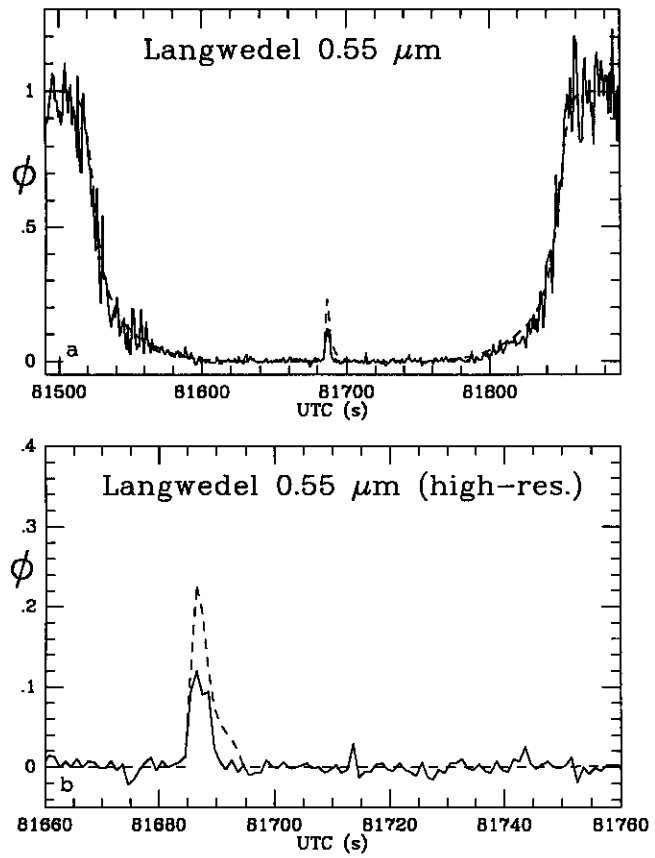

Fig. 11. Data and model for Langwedel

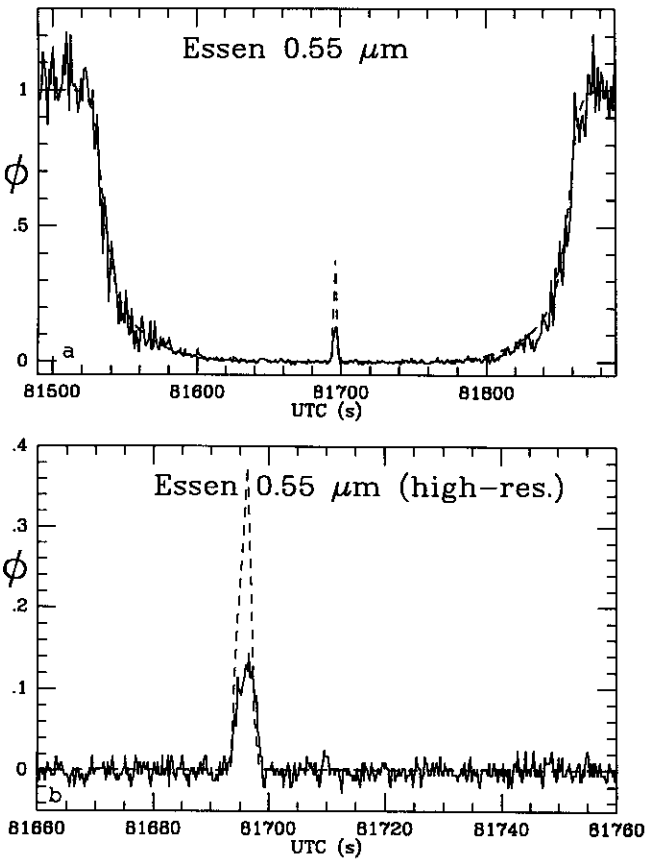

Fig. 12. Data and model for Essen

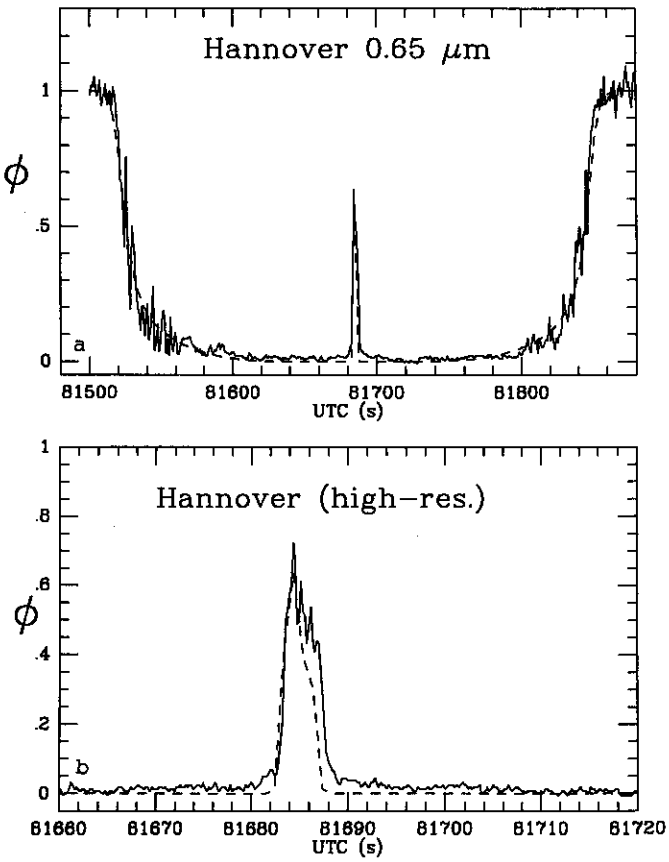

Fig. 13. Data and model for Hannover

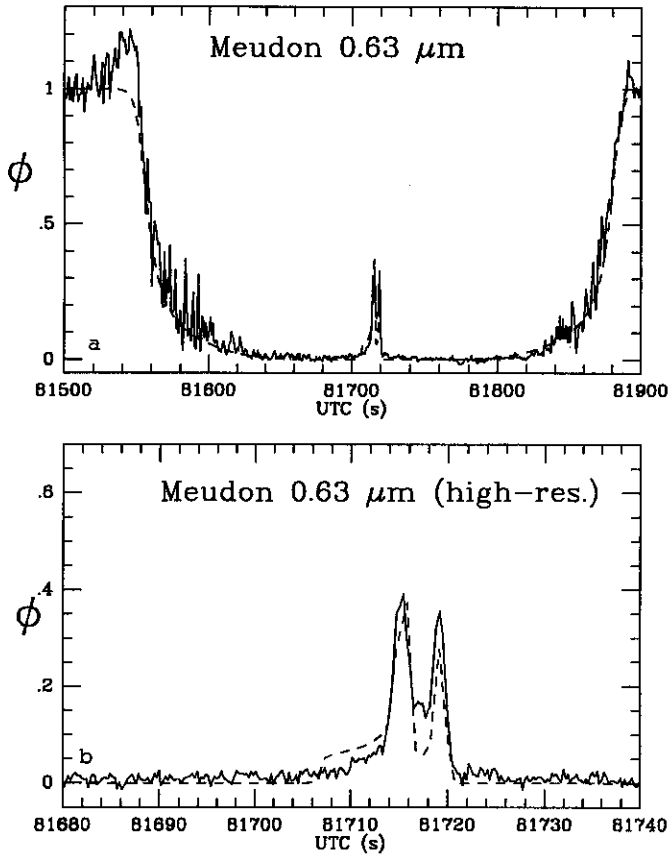

Fig. 14. Data and model for Meudon 1 m telescope

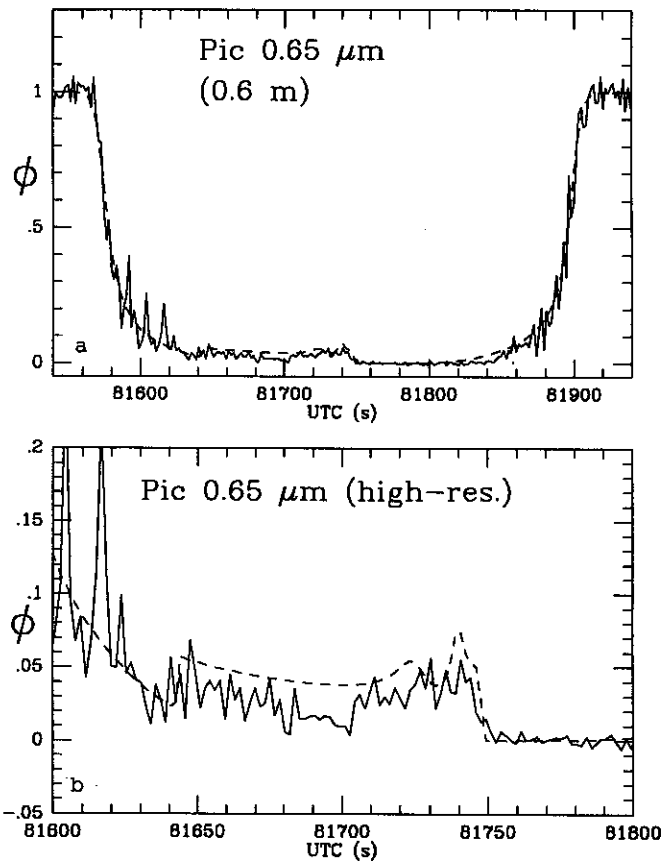

Fig. 16. Data and model for Pic du Midi 0.6 m telescope

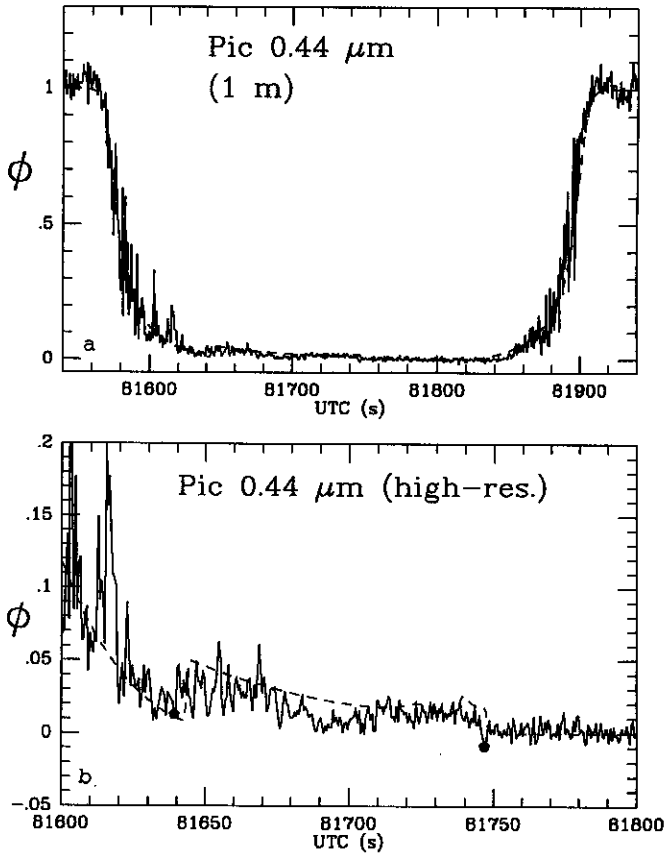

Fig. 15. Data and model for Pic du Midi 1 m telescope

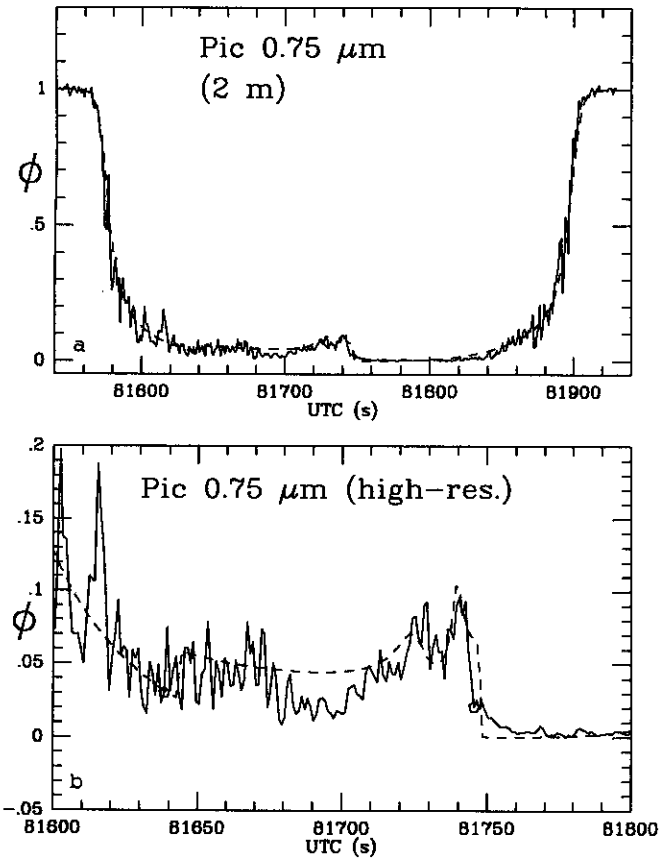

Fig. 17. Data and model for Pic du Midi 2 m telescope, 0.75 μm channel

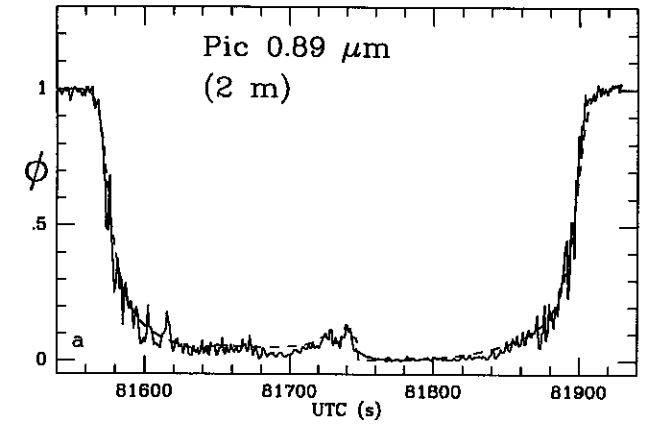

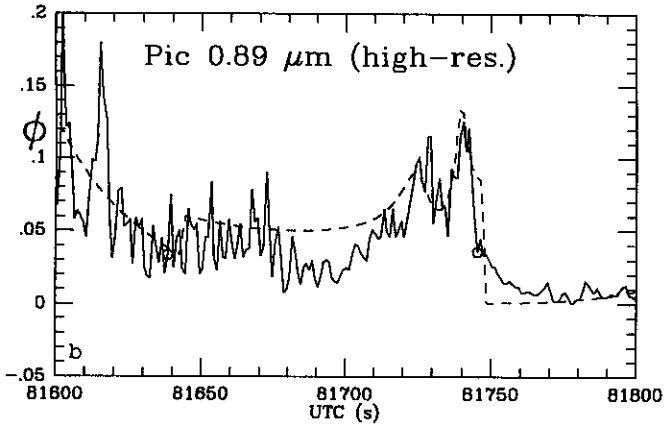

Fig. 18. Data and model for Pic du Midi 2 m telescope, 0.89 μm channel

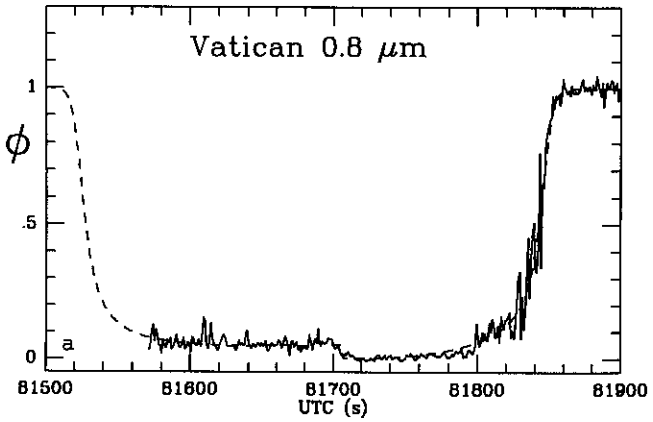

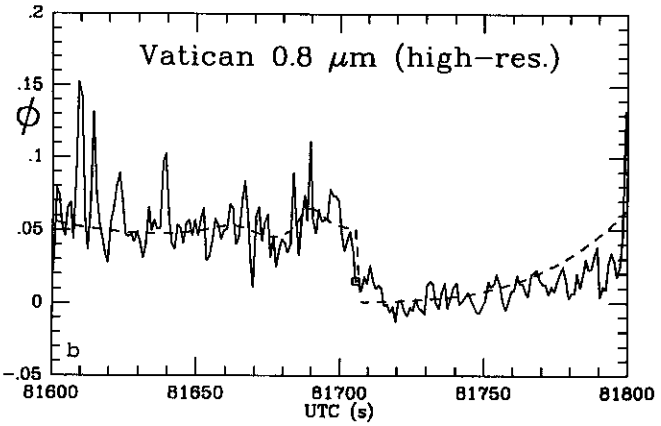

Fig. 20. Data and model for Vatican, red channel

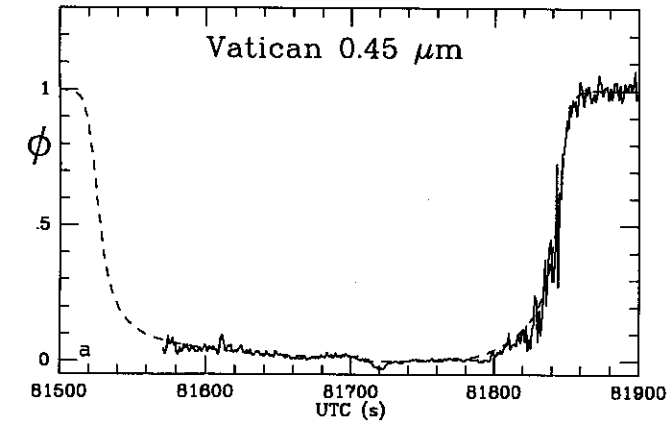

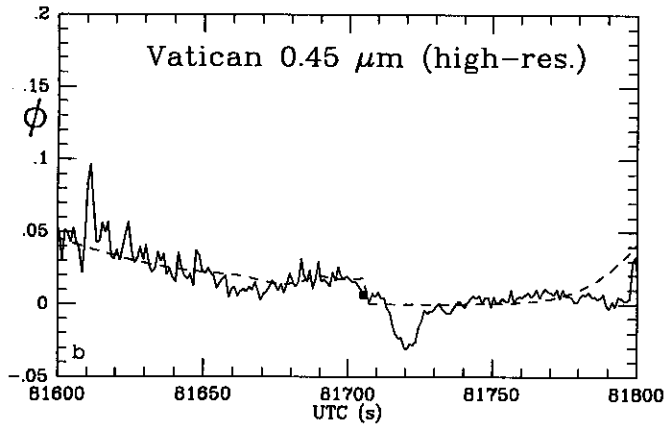

Fig. 19. Data and model for Vatican, blue channel. Immersion was obscured by clouds

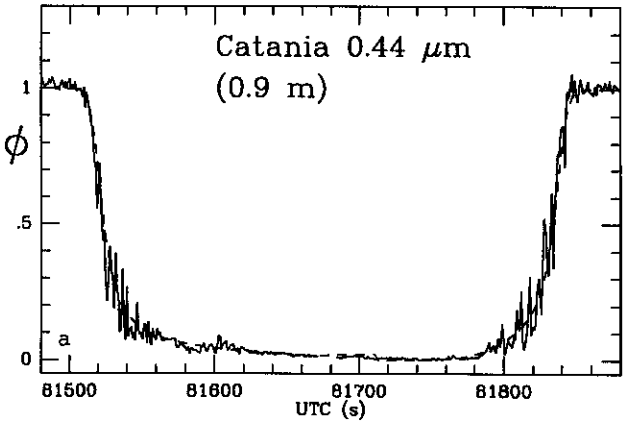

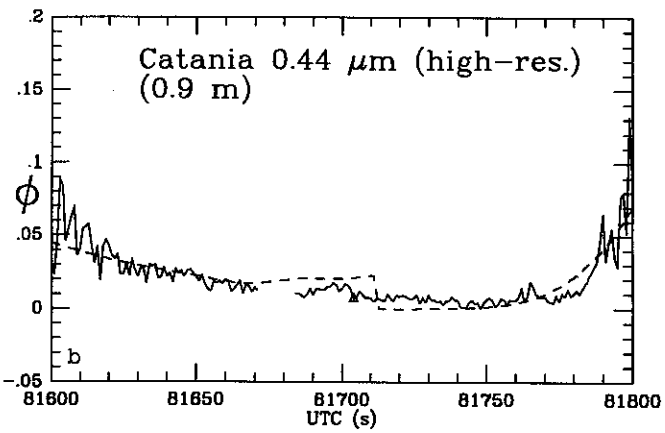

Fig. 21. Data and model for Catania 0.9 m, V channel

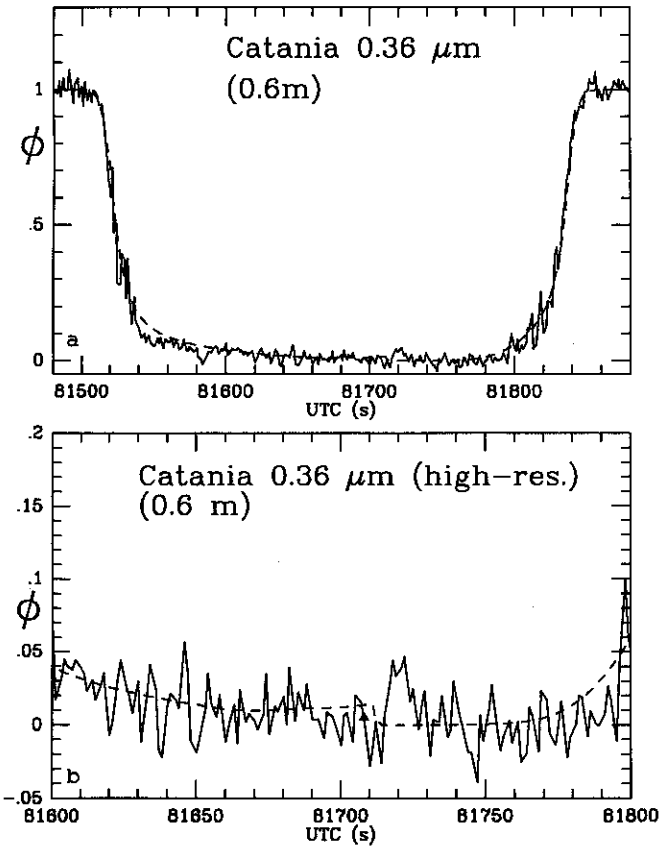

Fig. 22. Data and model for Catania 0.6 m, U channel

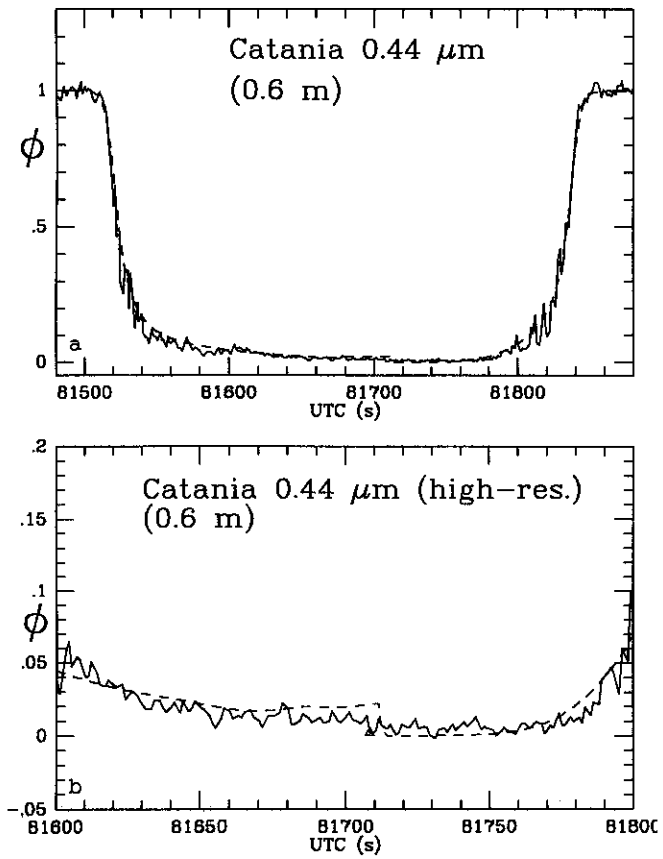

Fig. 23. Data and model for Catania 0.6 m, B channel

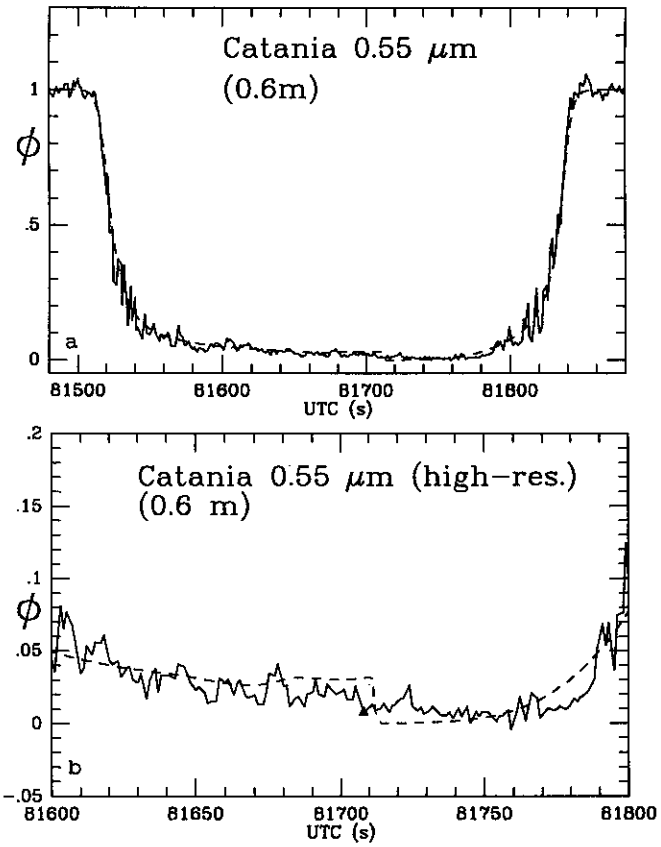

Fig. 24. Data and model for Catania 0.6 m, V channel

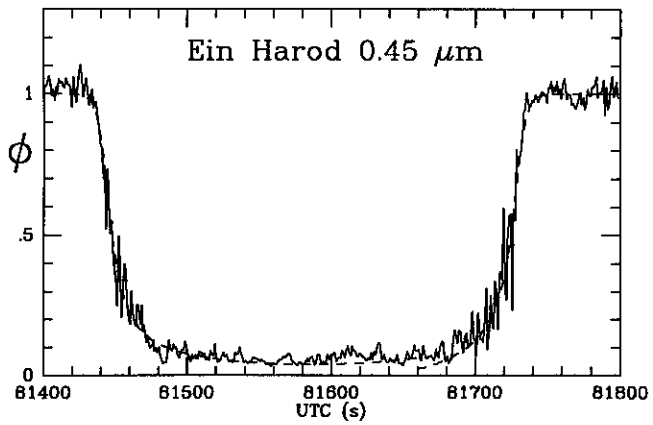

Fig. 25. Data and model for Ein Harod, blue channel

7 illustrates, this is caused by much larger obscuration of the principal stellar image in the northern haze layer than in the southern.

A second major effect is on the central caustics, where those caustics corresponding to limb points in the dense northern haze layer are essentially absent. This point is addressed in more detail in Sect. 5.

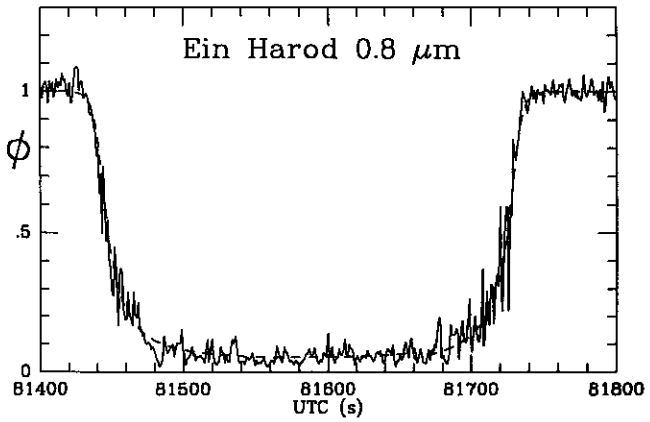

Fig. 26. Data and model for Ein Harod, red channel

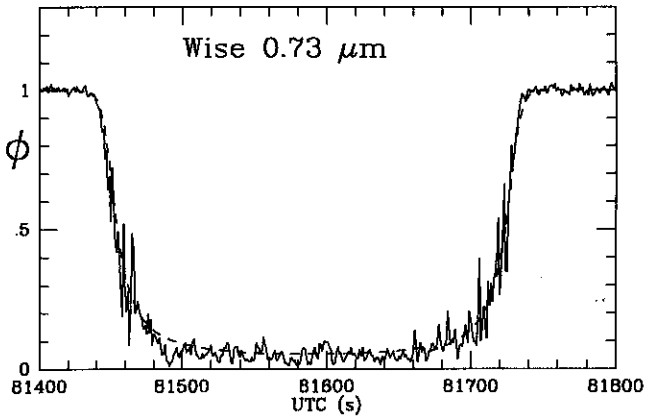

Fig. 27. Data and model for Wise

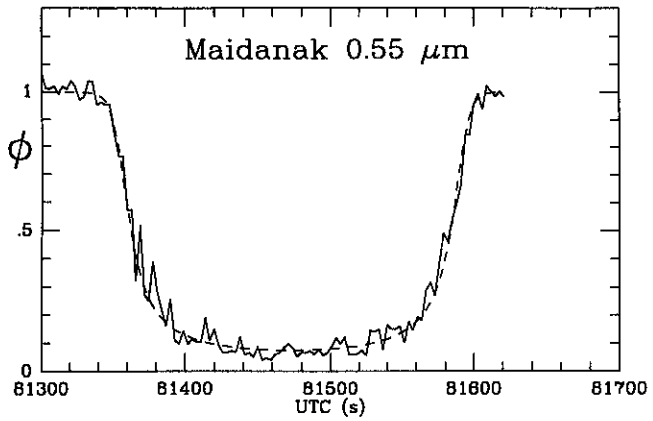

Fig. 28. Data and model for Maidanak

4.4. Inference of haze particle composition and size

The wavelength dependence of the extinction measured by the occultation ($\tau \propto \lambda^{-q}$, $q \sim 1.7$) implies that the aerosols have a size comparable to the wavelength (Mie scattering regime). This dependence may be used in principle to derive the mean radius of the particles at the altitude probed by the flashes. In practice, however, we find that all of a family of size distributions give the same wavelength dependence, i.e. the same value for the exponent q. Namely, we adopt a log normal size distribution (Hansen & Travis 1974) with a mean radius r_g and a standard deviation σ_g, i.e. the number of particles per unit radius interval $\propto \exp\left[-ln^2(r/r_g)/2\sigma_g^2\right]$.

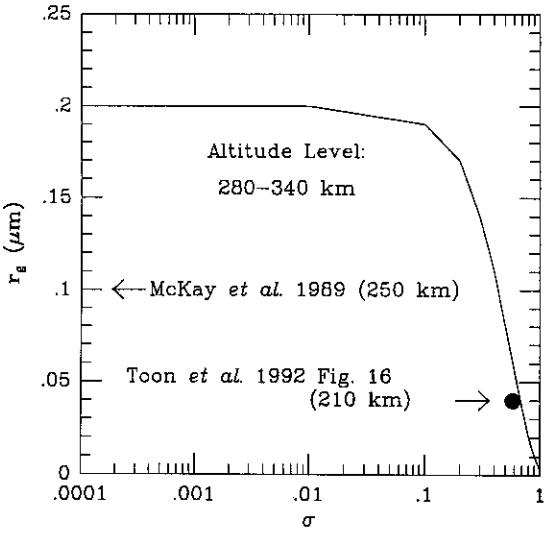

Fig. 29. Relation between mean grain radius r_g and size distribution standard deviation σ_g, as constrained by 28 Sgr data. Grain radius values at lower altitudes obtained by other investigators are also shown

This analysis is summarized in Fig. 29, where we have plotted, for each value of σ_g, the value of r_g which yields the $\lambda^{-1.7}$ dependence that we find for the optical depth. We assume that the aerosols are Mie scatterers, and we use the optical properties of tholins (Khare et al. 1983) with the imaginary index of refraction scaled by 4/3 as suggested by geometric albedo measurements (McKay et al. 1989). The resulting points shown in Fig. 29 are not sensitive to the precise value of the optical constants. For example, increasing or decreasing the imaginary index of Khare et al. in the visible by one order of magnitude does not significantly affect the result. Also, attempts have been made to change the dependence of the imaginary index, which varies like $\sim \lambda^{-4}$ in the visible and near infrared (0.4 to 1 μm) according to Khare et al. Other dependences, of the form $\lambda^{q'}$ were used for the imaginary index, but it was soon realized that changing the log-log slope q' up to -1 has little effect on the final log-log slope q derived for $\tau \propto \lambda^{-q}$.

On the other hand, Fig. 29 shows that the mean particle radius is somewhat sensitive to the width of the aerosol size distribution; for example a distribution characterized by $\sigma_g = 0.7$ requires $r_g = 0.035$ μm to fit the data, while one characterized by $\sigma_g = 0.3$ requires $r_g = 0.14$ μm. The maximum mean particle radius, corresponding to a monodisperse distribution ($\sigma_g = 0$), is then close to 0.2 μm. These conclusions apply to the 320-340 km altitude region in the northern hemisphere and to the 280-320 km region in the south, where the tangential optical depth due to aerosol extinction is on the order of 1 and the corresponding vertical optical depth is on the order of 0.05.

A mean particle radius of 0.1 μm has been derived from Pioneer 11 polarization measurements (Tomasko & Smith 1982),

while Voyager 1 measurements of brightness variations with phase angle suggest a mean particle radius of 0.2 μm or greater (Rages et al. 1983). Tomasko & Smith (1982) have attempted to explain this apparent contradiction between Pioneer and Voyager results by adding a thin layer of larger particles with vertical optical depth of 0.05 above a more extensive distribution of small particles. The results reported here appear to rule out this suggestion because the small particle size derived from the occultation measurement pertains precisely to the optical depth region in which Tomasko & Smith require large particles. West & Smith (1991) proposed an alternate explanation and suggested that the Voyager and Pioneer results could be reconciled if the aerosols are aggregates of smaller particles. The polarization properties of the aggregates are similar to those of small spherical scattering centers composing the aggregate while the scattering phase function is dominated by the overall size of the aerosol. Further work is required to determine if these aggregate particles are consistent with the wavelength dependence of extinction inferred from the occultation data. Finally, a recent paper by Toon et al. 1992, presents a revised model of Titan's aerosols. This model takes into account the UV, visible and IR measurements of the satellite geometric albedos, as well as some dynamical constraints to maintain the detached aerosol layer observed around 350 km by RP (upward winds at altitudes above 300 km). Toon et al. derive an approximately log normal size distribution for the aerosols at the 210 km altitude level, i.e. about 1-2 scale heights below the levels we probe here. Their Fig. 16 gives $\sigma_g \sim 0.58$ and $r_g \sim 0.04$ μm at that level. The corresponding point has been plotted in Fig. 29, and shows good agreement with our points, even though we are studying levels separated by 50 to 100 km in height.

Thus, our results appear to be consistent with the various observations and models of Titan's aerosols. Even though we cannot distinguish between these models, the results shown in Fig. 29 nevertheless yield important constraints on the aerosol distribution size in the 280-340 km altitude range. As stated earlier, this is because the points of Fig. 29 are directly derived from multiwavelength observations, and are rather model independent, since their positions are quite robust against the assumed optical properties of the grains.

5. Titan's central flash

All of the data sets from near-central chords clearly show the presence of a central flash produced by proximity to limb caustics. The stations that show this phenomenon (Meudon, Essen, Langwedel, RGO, Manley, and Hertford) span a distance of approximately 150 km parallel to Titan's projected spin axis. The flash has a width of about 100 km at the southernmost station (Meudon), but persists over a substantially larger distance in the orthogonal direction.

The original theory of the central flash produced by a nonspherical planetary atmosphere was derived by Elliot et al. (1977), motivated by observations from a single station of a flash produced by Mars' atmosphere during the occultation of ϵ Gem. This theory assumes that the atmospheric shape corresponds to an ellipsoid of rotation, as would be produced by slow, uniform rotation of the atmosphere. The flash is observed on the shadow plane at points corresponding to centers of curvature of the projected atmosphere. For an atmosphere with an elliptical projection, the locus is an equilateral diamond-like figure with the cusps aligned along the projected spin axis and orthogonally. Our 28 Sgr data cannot be satisfactorily fitted with such an equilateral central caustics pattern. As we sweep across this locus, there is a relation between the temporal duration of the flash observed at a single station which passes through the center of the shadow, and the change in duration and intensity of the flash for stations progressively farther from the center of the shadow. The maximum width of the central flash at Meudon, the station which exhibits a double flash, is too small to be consistent with the large distance from Meudon to Manley, the northernmost station which also shows a flash. Thus, caustics formed by Titan's southern limb do not coincide with the simple diamond-shaped locus produced by an elliptical limb, but are relatively more extended parallel to the spin axis, and more contracted perpendicular to the spin axis. No plausible distribution of Titan hazes could so distort the caustics observed by the six northernmost stations, which sample the relatively haze-free southern polar atmosphere. Hazes can truncate caustics, but cannot appreciably change their shape.

5.1. *Uniform rotation vs. differential rotation*

Apart from the disagreement with the data, there exists a physical basis for rejecting the model of a globally elliptical (oblate) Titan atmosphere, namely, the implied differential rotation velocities of the atmosphere are too large to be plausible. The oblate model that comes closest to fitting the data has an observed oblateness (i.e., projected in the reference plane) $e_{\rm obs} = (a - b_{\rm obs})/a = 0.016$, where a and $b_{\rm obs}$ are respectively the equatorial radius and the polar radius projected in the reference plane. This model has a diamond-shaped central caustic locus with each of the four cusps at a distance $2e_{\rm obs}a \approx 100$ km from the center of the shadow (Fig. 30). The oblateness of level surfaces of an atmosphere in hydrostatic equilibrium rotating at angular rate ω is given by

$$e = \frac{3}{2}J_2 + \frac{1}{2}\frac{a\omega^2}{g}, \tag{6}$$

where J_2 is Titan's dimensionless mass quadrupole moment, g is its atmospheric gravity (about 1 m/s^2), and $e = (a - b)/a$, where b is the true polar radius. We expect the solid body of Titan to be rotating synchronously with Titan's orbital period (16 days); thus the hydrostatic structure of the solid body should be spherically symmetric to within a few hundred meters, and we set $J_2 = 0$. Equation (6) can then be solved for ω using $e = 0.020$ (corresponding to $e_{\rm obs} = 0.016$), giving a maximum zonal flow velocity $\omega a = 340$ m/s, which is highly supersonic with respect to the solid surface. At a temperature of 170 K, the adiabatic sound speed in nitrogen gas is 266 m/s.

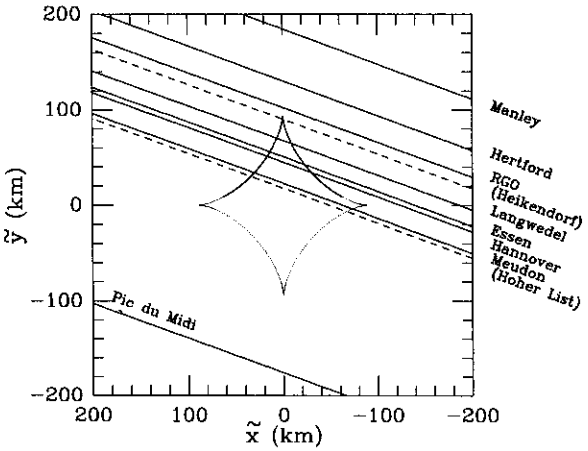

Fig. 30. The best-fit model for central caustics in the reference plane, assuming a simple oblate model for Titan's atmosphere. Portions of the caustics shown with light lines are missing because of large haze optical depth in Titan's northern hemisphere. *Dashed chords* show paths of stations with nonphotometric data. The coordinates $\tilde{x}, \tilde{y}$ are equivalent to x, y, but are rotated so that Titan's projected spin axis lies along the $\tilde{y}$ axis

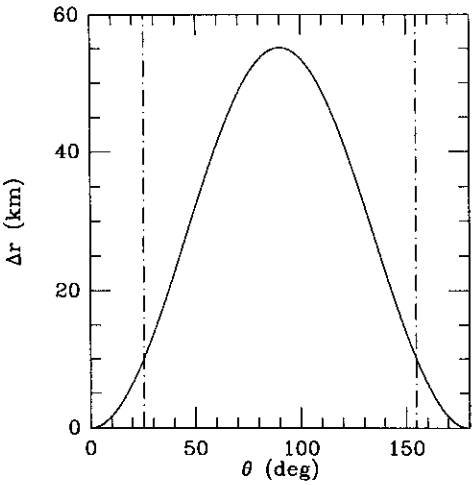

Fig. 31. *Solid curve*, difference in radius of a level surface in Titan's stratosphere, as a function of colatitude θ (angular distance from true spin axis), inferred from the best-fit simple oblate model. *Vertical dashed-dot lines* delimit the range of θ near the pole where no occultation data are available, because of the tilt of Titan's spin axis to the reference plane

Our discussion of the formation of Titan's central flash will require the use of three-dimensional coordinates centered on Titan. We let $\mathbf{r}_3$ be the three-dimensional vector position of a point in Titan's atmosphere with respect to the center of Titan; $\mathbf{r}$ is its two-dimensional projection onto the reference plane. We will use a spherical polar coordinate system (r_3, θ, φ), where r_3 is the distance from the center of Titan, θ is the angle from the spin axis (colatitude), and φ is the angle from an arbitrary longitude.

Figure 31 shows Δr, the deviation of the atmosphere from spherical structure, defined by $\Delta r = r_3(\theta) - b$, for both the projected and unprojected models. Zonal flow velocities $v = r_3\omega \approx a\omega \sin\theta$ are shown in Fig. 32.

Since the structure of the central caustics depends essentially on the curvature of the atmosphere, we seek a more general theory to relate the shape of the atmosphere to the zonal wind distribution on Titan. Our problem is to find a wind distribution which is physically plausible and which reproduces the observed geometry of the central caustics.

Assume that the only winds which are important for this problem are steady-state zonal flows with velocity $\mathbf{v} = r_3\omega(r_3, \theta)\,\mathbf{e}_\varphi$, where $\mathbf{e}_\varphi$ is a unit vector in the direction of increasing φ. The underlying planet, and hence the gravity field, is assumed to be spherically symmetric. Viscosity is set equal to zero. The two components of Euler's equation then read:

$$\frac{1}{\rho}\left(\frac{\partial P}{\partial \theta}\right)_{r_3} = r_3^2\omega^2 \sin\theta\cos\theta \tag{7}$$

(θ-component), and

$$\frac{1}{\rho}\left(\frac{\partial P}{\partial r_3}\right)_{\theta} = -g + r_3\omega^2 \sin^2\theta \tag{8}$$

(r_3-component), where P is the pressure and ρ is the mass density.

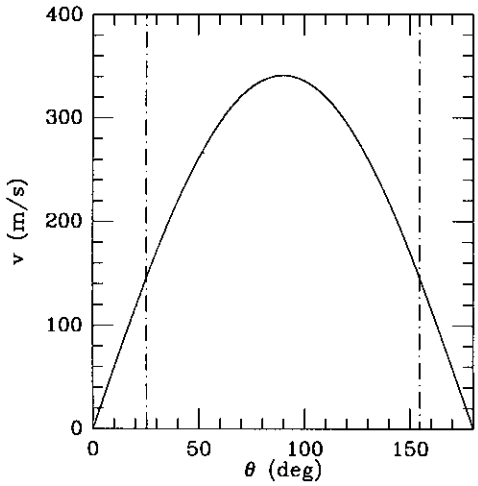

Fig. 32. Zonal flow velocity in Titan's stratosphere, as a function of colatitude θ, inferred from the best-fit simple oblate model. *Vertical dashed lines* delimit the range of θ near the pole where no occultation data are available, because of the tilt of Titan's spin axis to the reference plane

For an isothermal or nearly-isothermal atmosphere, the caustics are determined by the shape of surfaces of constant N, which coincide with isopycnic surfaces (constant ρ) for constant chemical composition. Let the radius of an isopycnic surface with polar radius b be given by

$$r_3 = b[1 + f(b, \theta)], \tag{9}$$

where f is a small quantity of order $b\omega^2/g$, vanishing at the pole ($\theta = 0$). We transform Eqs. (7) and (8) from the variables r_3, θ to the new variables b, θ, and linearize in f and ω^2, with the result

$$\frac{1}{\rho}\left[\left(\frac{\partial P}{\partial \theta}\right)_b - b\left(\frac{\partial f}{\partial \theta}\right)_b\left(\frac{\partial P}{\partial b}\right)_\theta\right] = b^2\omega^2 \sin\theta\cos\theta \tag{10}$$

(θ-component), and

$$\frac{1}{\rho}\left(\frac{\partial P}{\partial b}\right)_\theta = -g_b\left[1 - f + b\left(\frac{\partial f}{\partial b}\right)_\theta\right] + b\omega^2 \sin^2\theta \tag{11}$$

(r_3-component), where $g = GM/r_3^2 \approx (1-2f)GM/b^2 = (1-2f)g_b$.

Now substitute for P the ideal-gas equation of state $P = R\rho T/\mu$. The atmosphere is assumed to be at temperature $T = T_0 + \Delta T(b,\theta)$, where ΔT is assumed to be small compared with the constant background temperature T_0. Define a gas scale height $H = RT_0/\mu g_b$, and a rotation parameter $q(b,\theta) = b\omega^2/g_b$. Expand $f, \Delta T$, and q on a basis set of Legendre polynomials $P_l(\cos\theta)$:

$$f = \sum_{l=0}^{\infty} f_l(b) P_l(\cos\theta), \tag{12}$$

etc. By definition,

$$f_0 = -\sum_{l=1}^{\infty} f_l. \tag{13}$$

Eqs. (10) and (11) then yield the following hierarchies:

$$f_l + \frac{H}{b}\frac{\Delta T_l}{T_0} = -\sum_{m=0}^{\infty} A_{lm} q_m, \tag{14}$$

and

$$H\left(\frac{d\Delta T_l/T_0}{db}\right) - \frac{\Delta T_l}{T_0} - f_l + b\left(\frac{df_l}{db}\right) = \sum_{m=0}^{\infty} B_{lm} q_m \tag{15}$$

($l \neq 0$), where

$$A_{lm} = \frac{2m+1}{2}\int_{-1}^{1} dx P_m(x) \int_0^x dx' x' P_l(x') \tag{16}$$

and

$$B_{lm} = \frac{2m+1}{2}\int_{-1}^{1} dx P_m(x) P_l(x)\left[\frac{2}{3} - \frac{2}{3}P_2(x)\right] \tag{17}$$

are dimensionless projection coefficients, which have the property that they are zero unless l and m are both even (or both odd). In obtaining Eq. (15), we have used the lowest-order result for the unperturbed atmosphere at temperature T_0, $d\rho/db = -\rho/H$. For solid-body rotation and $\Delta T = 0$, eqs. (14) and (15) reduce to $f_2 = -q_0/3$ and $f_2 - bdf_2/db = 2q_0/3$, giving solution (6) with $J_2 = 0$. For the more general case of arbitrary temperature gradients and zonal wind profiles, hierarchies (14) and (15) couple these quantities with the atmospheric shape coefficients f_l as a function of height b. If temperature fluctuations ΔT can be ignored, hierarchy (14) can be straightforwardly inverted to deduce the zonal wind profile coefficients q_m from the shape coefficients f_l. For Titan's atmosphere in the region of interest, $H/b \approx 0.017$, while the inversions presented in Sect. (3) suggest that $\Delta T/T_0 \approx 0.1$ in the pressure range of a few tens of microbars. In reality this represents an upper limit on $\Delta T/T_0$ since the presence of strong scintillations introduces spurious detail in the temperature profiles obtained from inversions. We have no direct information about the temperature fluctuations at $P \approx 100$ μbar where the central flash is formed, but we shall assume that they are similar to those at higher levels. We further assume that the shape coefficients f_l vary with b only over scales of order b. Thus they can be treated as constant in the relatively thin height range probed by the occultation, and hierarchy (15) then plays no role in the solution. Ultimately, of course, if the atmosphere becomes stationary and spherically symmetric with respect to the solid surface at deeper layers, appreciable temperature gradients must play a determining role in the hierarchies (14) and (15). We assume that this occurs deeper in the atmosphere than the layers of interest to us here.

We may thus introduce a general set of shape coefficients f_l to yield a central caustic pattern which agrees with the observations. However, in the absence of temperature gradients, the function $f(\theta)$ must obey a strict constraint. If T = const., we have $(\partial P/\partial\theta)_b = 0$, and from Eq. (11), $(\partial P/\partial b)_\theta = -g_b\rho$ to lowest order. Substituting in Eq. (10), we obtain

$$2\left(\frac{\partial f}{\partial\theta}\right)_b / \sin 2\theta = q = b\omega^2/g_b \geq 0, \tag{18}$$

for all θ. This requires that $\partial f/\partial\theta$ be an odd function of θ, and thus that f be an even function of θ. This restricts the expansion to only even terms in l, and is a consequence of the general Poincaré-Wavre theorem (Tassoul 1978).

To obtain a central flash of the required geometry and dimensions, and to simultaneously satisfy constraint (18), we require an expansion for f in which the even coefficients f_{2l} are all negative, and decrease more slowly with increasing l than would be the case for an elliptical profile. It must also be recognized that the coefficients for the observed profile,

$$r = b_{\rm obs}(1 + f_{\rm obs}), \tag{19}$$

are not the same as the coefficients of the expansion about the rotation axis, Eq. (9), because the rotation axis is tilted to the reference plane by an angle $B = 25.4°$. Because of the tilt, the shape of the satellite's atmosphere at any colatitude smaller than B from the poles is unobservable by occultation, and the true polar radius b increases to the apparent polar radius $b_{\rm obs}$ in the reference plane. Define a cartesian coordinate system x_3, y_3, z_3 with the y_3-axis along Titan's rotation axis, and the z_3-axis in the plane defined by the spin axis and the vector from Titan to 28 Sgr. The "true" coefficients f_{2l} give the atmospheric shape in this coordinate system:

$$r_3 = b\left[1 - \sum_{l=1}^{\infty} f_{2l} + \sum_{l=1}^{\infty} f_{2l} P_{2l}(y_3/r_3)\right]. \tag{20}$$

Now transform to a new coordinate system $\tilde{x}, \tilde{y}, \tilde{z}$ by rotating about the x_3-axis by angle B:

$$\begin{aligned} x_3 &= \tilde{x}, \\ y_3 &= \tilde{y}\cos B - \tilde{z}\sin B, \\ z_3 &= \tilde{z}\cos B + \tilde{y}\sin B, \end{aligned} \tag{21}$$

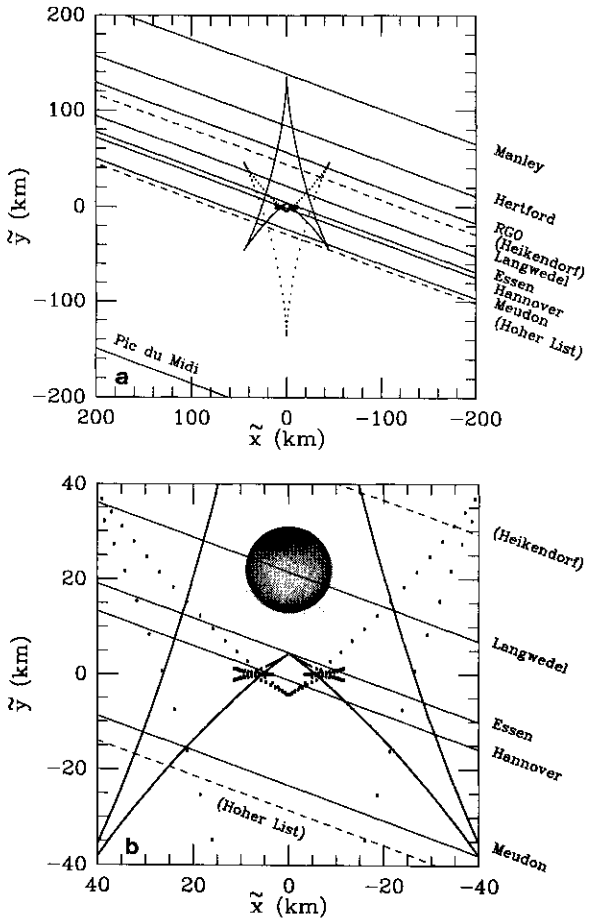

Fig. 33. (a) The best-fit model for central caustics in the reference plane, assuming a differentially-rotating model for Titan's atmosphere. Portions of the caustics shown with dotted lines are missing because of large haze optical depth in Titan's northern hemisphere. *Dashed chords* show paths of stations with nonphotometric data (Heikendorf, Hoher List). (b) Enlargement of the central region of (a). *Shaded circle* shows 28 Sgr's disk projected on the reference plane, with a radius = 9 km (Hubbard et al. 1992). Details of caustics at smaller scales are smeared out

and substitute in Eq. (20). If the projected radius of a point in the atmosphere is $r = \sqrt{\tilde{x}^2 + \tilde{y}^2}$, then the location of the point of tangency to the atmosphere is given by $\partial r/\partial \tilde{z} = 0$ (the partial is taken with $\tilde{y}$ held constant, and staying on the constant-density surface), with the result (to lowest order in f):

$$\tilde{z} = b \sum_{l=1}^{\infty} f_{2l} P'_{2l}(\tilde{y} \cos B/b) \sin B. \qquad (22)$$

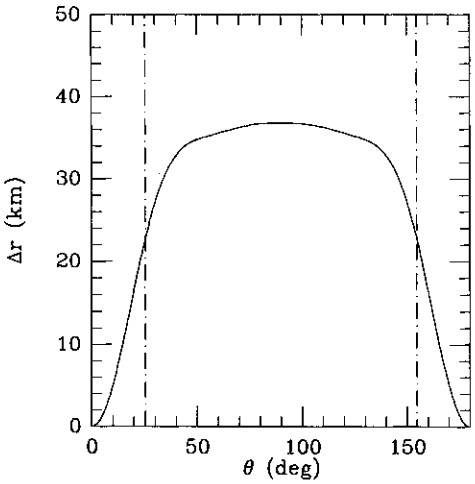

Fig. 34. *Solid curve*, difference in radius of a level surface in Titan's stratosphere, as a function of colatitude θ, inferred from the best-fit differentially-rotating model. *Vertical dashed-dot lines* delimit the range of θ near the pole where no occultation data are available, because of the tilt of Titan's spin axis to the reference plane

Setting $\tilde{z} = 0$ to lowest order, from Eq. (22), it follows that $r_3 = r$, and, from Eq. (21), $y_3 = \tilde{y} \cos B$, which gives

$$r = b\Big[1 - \sum_{l=1}^{\infty} f_{2l} + \sum_{l=1}^{\infty} f_{2l} P_{2l}(\cos\tilde{\theta} \cos B)\Big], \qquad (23)$$

where $\cos\tilde{\theta} = \tilde{y}/r$. The observed shape coefficients $f_{2l,\mathrm{obs}}$ are then obtained as a linear combination of the "true" coefficients f_{2l} by projecting expansion (23) onto the basis $P_{2l}(\cos\tilde{\theta})$. The inverse process of obtaining the "true" shape from the observed shape involves an extrapolation of the shape components into the unobservable region within an angle B of the pole.

After considerable experimentation, we have derived a pattern of central caustics with an aspect ratio which matches the data (see Fig. 33). This is computed with expansion coefficients given in Table 4. The series is truncated after $f_{8,\mathrm{obs}}$. These coefficients are then deprojected by inverting series (23) to obtain the coefficients with respect to the rotation axis, which are also given in Table 4. These coefficients give the deprojected deviations of the atmosphere from spherical symmetry Δr (Fig. 34). Finally, the system of equations (14) is inverted (with $\Delta T_l = 0$) to obtain the zonal flow profile (Fig. 35).

Note that the atmospheric model with nonuniform ω differs only slightly from radial symmetry except near the poles. Since the geometry of Titan's orientation with respect to the reference plane prevents us from measuring the atmospheric shape within

Table 4. Expansion coefficients for the shape of Titan's stratosphere

rotation model	f_0	f_2	f_4	f_6	f_8
uniform, observed	0.01	-0.01	0	0	0
uniform, deprojected	0.012255	-0.012255	0	0	0
nonuniform, observed	0.00399	-0.00185	-0.00111	-0.00074	-0.00030
nonuniform, deprojected	0.01090	-0.00445	-0.00363	-0.00216	-0.00067

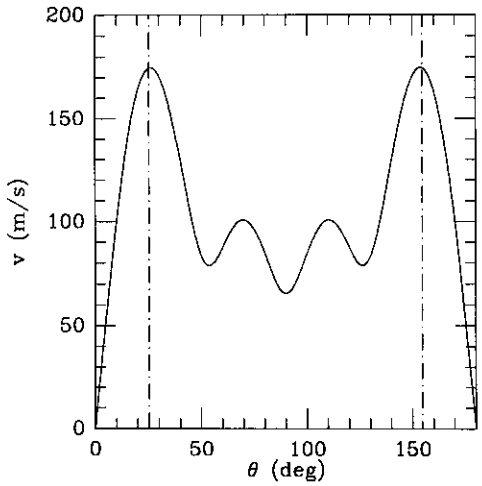

Fig. 35. Zonal flow velocity in Titan's stratosphere, as a function of colatitude θ, inferred from the best-fit differentially-rotating model. *Vertical dashed lines* delimit the range of θ near the pole where no occultation data are available, because of the tilt of Titan's spin axis to the reference plane

an angular distance B of the pole, the deprojected shape is an extrapolation of the projected shape within this region, and may therefore be an exaggeration of the true deviation from spherical symmetry. The high-order variations in the zonal velocity field are artifacts of the truncation of the expansion at P_8. Thus, the inferred zonal velocities are to be interpreted in a qualitative and not quantitative sense. It is interesting to note, however, that the high-order terms that we have introduced into Titan's atmospheric shape produce high-order variations in the model lightcurves near the center of the shadow which are not in contradiction to the data (see especially the lightcurves for Pic du Midi and Vatican). We also note that the model for Titan's zonal circulation was derived entirely from the occultation data set, without reference to any global circulation model (GCM). In fact, however, our result shown in Fig. 35 agrees both qualitatively and quantitatively with a Titan GCM published by Hourdin et al. (1992; see especially their fig. 6). Our model and the GCM were developed completely independently.

Finally, we can compare the altitude of the isopycnic surface in Fig. 34 with the altitude of the detached haze layer as derived by RP. These authors derive an oblate shape, aligned with Titan's assumed spin axis, for the loci of the densest parts of this layer. They give an altitude of 357 ± 5 km for the layer near the equator, and 340 ± 10 km near the pole (77.5° latitude). Figure 34 gives an altitude difference ~ 27 km between these two latitudes. Although we are measuring a different physical quantity (isopycnic level instead of maximum of optical depth), it is interesting to note that our results are consistent with those of RP.

We conclude the following: (a) A reasonable central flash having the size and aspect ratio necessary to fit the data can be obtained with differential zonal flows with velocities on the order of 100 m/s. We emphasize that this result is valid only to order of magnitude because of the sensitivity of the inversion to the values of the shape coefficients, which are uncertain to ±20 percent (estimated). (b) The central flash requires higher angular velocities near the poles than at equatorial latitudes. (c) The deprojected shape coefficients are of the order of a few $\times 10^{-3}$. Our estimate of the possible effects of temperature gradients indicates that they may begin to be important at the level of $\sim 10^{-3}$ in Eq. (8). Thus our assumption about the constancy of T on isopycnic surfaces may be only qualitatively valid.

5.2. *Implications of meridional temperature gradients for zonal winds*

The deprojected curve of geopotential height in Fig. 34 indicates that the height of the isopycnic surface at the central flash altitudes (~ 0.25 mbar) decreases approximately 14 km between the equator and 65° latitude. This equatorial "bulge" must be supported hydrostatically. Because the lateral contrasts in pressure near the surface are expected to be small (*cf.*, *e.g.*, Hunten et al. 1984), this implies that the temperature, integrated over a vertical column from the surface to the central flash level, must be warmer at low latitudes than at high. If $\Delta T(P)$ denotes the decrease in temperature along an isobar at pressure P from the equator to 65°, and $\Delta z(P)$ the corresponding decrease in isobaric height, then integration of Euler's vertical momentum equation (8) from the surface to pressure level P and from the equator to 65° latitude leads to the condition:

$$\Delta z(P) = \frac{R}{\mu} \int_P^{P_S} \Delta T(P') \frac{d \ln P'}{g}, \tag{24}$$

where R is the universal gas constant, μ is the molecular weight of the atmosphere, and P_S is the surface pressure. In deriving (24), use was made of the ideal gas law. Furthermore, the term representing the centripetal acceleration on the right-hand side of Eq. (8) was neglected relative to g, which is a good approximation for the wind speeds depicted in Fig. 35. The analysis in the preceding subsections assumed that there were no temperature gradients along isobars at the central flash altitudes, and

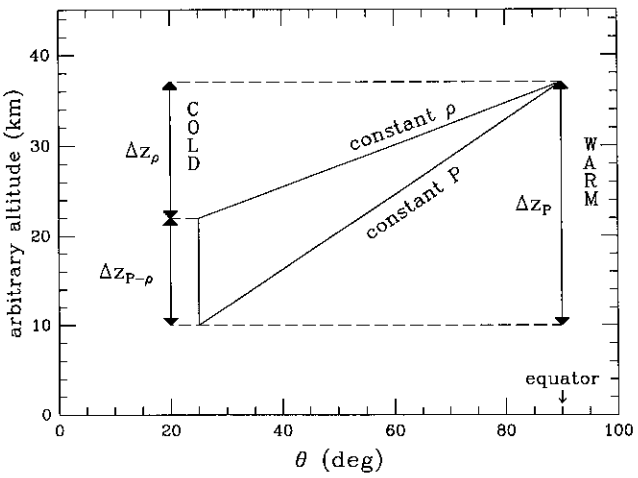

Fig. 36. Schematic of isobaric and isopycnic surfaces at the central flash altitudes when temperatures decrease poleward at these heights

hence that isobars and isopycnic surfaces coincided at these levels. However, observations by the Voyager spacecraft, taken eight years earlier near Titan's northern spring equinox, indicated that high latitudes remained colder up to the 0.3-mbar level or higher (Flasar et al. 1981; Flasar & Conrath 1990; Coustenis et al. 1991). If this situation also pertains to the present observations, then densities will increase poleward along isobars. Because the density decreases with altitude, this means that the isopycnic surface height will decrease poleward less rapidly than the isobaric height, as Fig. 36 illustrates. In general, the zonal winds are coupled to the decrease in isobaric height, not isopycnic height, and therefore the earlier calculation of the zonal winds would underestimate their strength under the conditions depicted in the figure. The magnitude of this effect depends on how confined the meridional temperature contrast is in altitude, as will now be shown.

In Fig. 36, the drop in isobaric height (Δz_P), the drop in isopycnic height (Δz_ρ), and their difference ($\Delta z_{P-\rho}$) are defined as positive quantities. From the ideal gas law, the fractional change in density along the 0.25-mbar isobar is simply $-\Delta T/T|_{P=0.25\,\mathrm{mbar}}$. Euler's vertical balance equation (8) and the ideal gas law imply the relation:

$$\frac{\partial z}{\partial \ln P} = -\frac{\frac{RT}{\mu g}}{1+\frac{R}{\mu g}\frac{\partial T}{\partial z}} = -\frac{RT}{\mu g}, \tag{25}$$

where the last step, omitting the term involving the vertical gradient in temperature, introduces an error of only a few percent at the altitudes of the central flash (*cf.* Lindal et al. 1983; Coustenis et al. 1991).

If the height $\Delta z_{P-\rho}$ is not too large, integration of Eq. (25) – together with the ideal-gas relation that $\Delta\rho/\rho = -\Delta T/T$ along isobars – simply yields $\Delta z_{P-\rho} = \frac{RT}{\mu g}\frac{\Delta T}{T}|_{P=0.25\,mbar}$. Combination with Eq. (24) gives

$$\frac{\Delta z_{P-\rho}}{\Delta z_P} = \frac{\Delta T_{P=0.25\,mbar}/g}{\int_P^{P_S}\Delta T(P')\frac{d\ln P'}{g}}. \tag{26}$$

The zonal winds depends on Δz_P; this is just a restatement of Euler's meridional balance equation (7), cast in terms of meridional geopotential gradients along isobars instead of meridional pressure gradients at constant height. The correction to the inferred winds is proportional to $\sqrt{\Delta z_P/\Delta z_\rho}$.

To examine the possible magnitudes of the divergence of the isobaric and isopycnic surfaces at the central flash altitudes, two limiting cases have been examined. The first assumes that $\Delta T(P) = 0$ at the surface and increases linearly with $-\ln P$. Neglecting the vertical variation in g, the left-hand side of Eq. (26) becomes $1/\frac{1}{2}\,ln\left(\frac{P_S=1.5\,bar}{0.25\,mbar}\right) = 0.23$. Thus $\Delta z_P/\Delta z_\rho \approx 1.29$, and the implied zonal winds are only 14% larger than estimated earlier. With $\Delta z_\rho = 14$ km from the observations, Eq. (24) implies that $\Delta T|_{P=0.25\,mbar} = 17$ K, which is comparable to the meridional temperature contrasts observed by *Voyager* (Flasar et al. 1981; Flasar & Conrath 1990; Coustenis et al. 1991). The *Voyager* observations suggest that ΔT may increase over a more restricted range of altitudes (Flasar et al. 1981). An extreme case is one in which $\Delta T = 0$ up to the 15 mbar level in the middle stratosphere, then increases linearly with $-\ln P$ at higher altitudes. This model implies $\Delta z_P/\Delta z_\rho \approx 2$ and winds which are 40% larger than estimated in the earlier subsection. The implied temperature contrast is $\Delta T|_{P=0.25\,mbar} \approx 56$ K, which is far larger than that observed by *Voyager* during northern spring. Hence, it would seem that the temperature contrasts – and the concomitant zonal winds – must build up more slowly with altitude than this extreme model suggests.

5.3. Sensitivity of central flash to spin axis

On 3 July 1989, the position angle of Saturn's projected spin axis with respect to celestial north (J2000.0 coordinates) was $p_S = 6.255°$. In the foregoing discussion we have assumed that p_T, the position angle of Titan's projected spin vector $\mathbf{e}_N$, was also p_S. In this section we set limits on the maximum difference between p_S and p_T.

Let $p_T = p_S + \Delta p$. Figure 3 and Figs. 8-28 are computed with $\Delta p = 0$. The central flash times at the northernmost stations indicate a sensitivity to Δp at the level of about $\pm 5°$, while the times of entry or exit into haze layers are sensitive to Δp at the level of about $\pm 1°$. As we have seen from Sect. 4, when the projected spin vector in the reference plane $\mathbf{e}_N$ is calculated under the assumption $\Delta p = 0$, the atmospheric north-south boundary between the haze domains as defined by $\tilde{\theta}_c$ turns out to be axisymmetric with $\mathbf{e}_N$ to within about one degree.

The central flash probes Titan's atmosphere at somewhat deeper layers than the boundary between the haze domains, and is sensitive to the axisymmetry of the isopycnic surfaces. Based on central flash calculations with varying values of Δp, holding all other parameters from the optimized solution constant, we conclude $\Delta p = 0° \pm 5°$.

If we calculate the characteristic time for the evolution of Titan's spin state under the influence of Saturn's tidal field, it turns out to be much less than the age of the solar system for any plausible choice of parameters. It is thus highly probable that the rotation period of Titan's solid body is equal to its orbital period, that the spin vector of Titan's solid body is collinear with Saturn's spin vector as defined by the ring plane, and that the axis of symmetry of the atmosphere aligns with the spin vector of the solid body.

5.4. A further consistency check

The Heikendorf and Hoher List stations suffered from nonphotometric conditions, and data from these sites were not analyzed during the initial modelling of lightcurves. However, as Figure 33 shows, both the Heikendorf and Hoher List chords passed close to the center of the caustics. The Hoher List chord was only slightly south of the Meudon chord, and the lightcurve would have played a crucial role in the analysis, since we would expect to see a double central flash as at Meudon. Figures 37 and 38 respectively show the Heikendorf and Hoher List lightcurves, plotted with theoretical lightcurves from our best-fit model. The observational lightcurves have been roughly scaled to permit

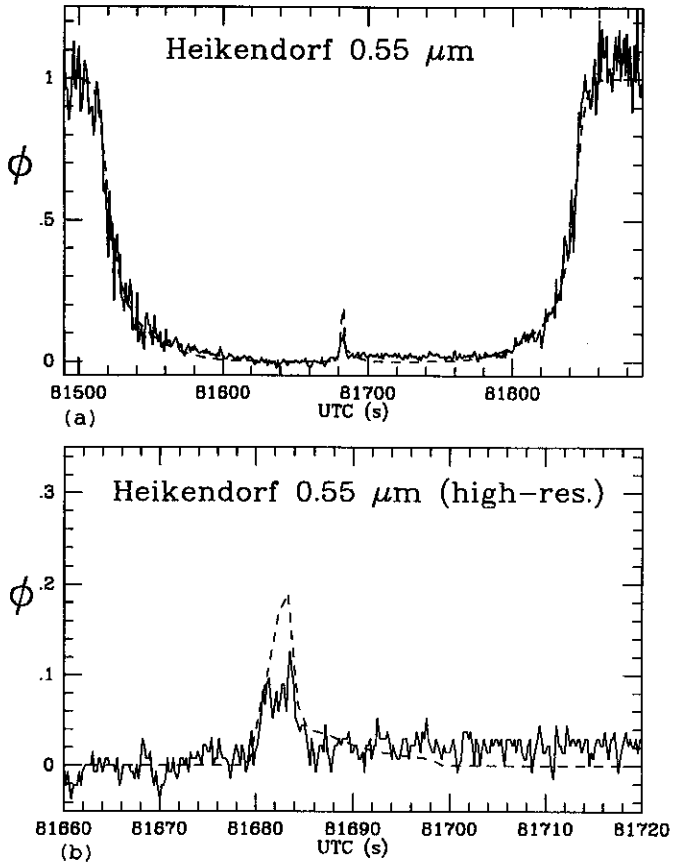

Fig. 37. Heikendorf data (*solid curve*), compared with the best-fit theoretical model (*dashed*). Excursions in the data baseline are evident

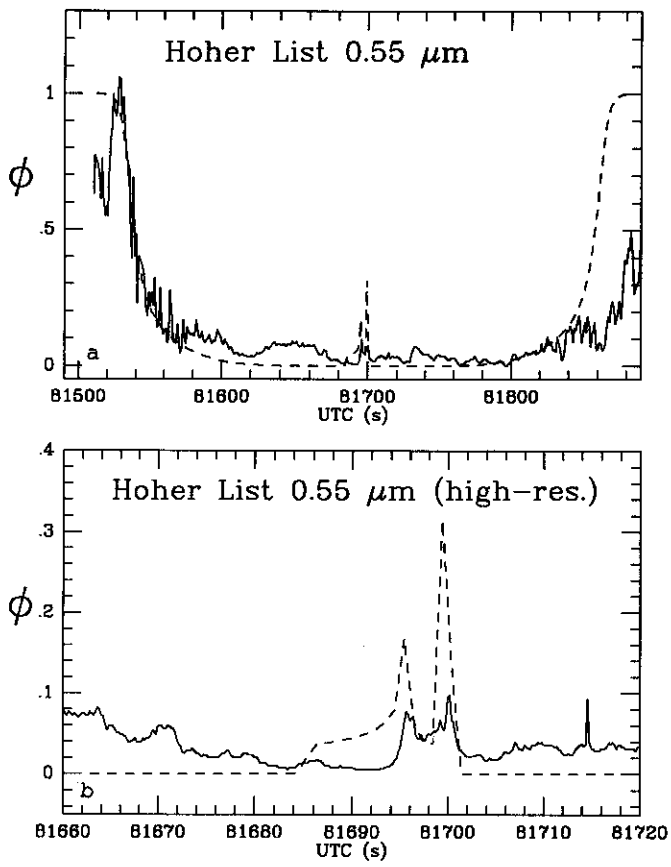

Fig. 38. Hoher List data (*solid curve*), compared with the best-fit theoretical model (*dashed*). Strong transparency variations and excursions in the data baseline are evident

comparison with the theoretical curves, but cannot be quantitatively normalized. Not only does the transparency vary, but the zero-flux baseline drifts up and down due to varying contributions of sky background and Titan background. In the case of the Hoher List data, a second channel which monitored another star shows that the transparency was essentially zero just prior to the central flash, but then rose to a value of about 0.5 during the central flash. A double central flash is indeed visible in the Hoher List data, and matches the theoretical profile. We emphasize that the Heikendorf and Hoher List data sets were examined only after the final theoretical model had been optimized to the other data.

6. Discussion

The pronounced difference in the high-altitude haze density between Titan's northern and southern hemisphere is a striking result of our synthesis. This difference has been noted previously from analyses of Pioneer and Voyager spacecraft data (Toon et al. 1992). We quote from Toon et al.: "The detached haze layer observed by Voyager (Smith et al. 1981) is present throughout the Southern hemisphere and at low latitudes of the Northern hemisphere. Its altitude is smaller at the south pole, and it merges with the main haze layer at the north pole. Hence, there is both a hemispheric asymmetry, and an equator to pole variation." They attribute the detached haze to large scale Hadley circulation at altitudes above 300 km, with vertical velocities ~ 0.01 m/s. In 1981, at the time of the Voyager encounter, according to this model, rising motions would have occurred in the southern hemisphere and equatorial regions, and sinking motions at middle and high northern latitudes. In 1981, Titan was near equinox, moving from northern winter to northern summer, whereas in 1989 it was near midsummer at northern latitudes. We observe a haze distribution which is virtually the opposite of that described by Toon *et al.*, which, if their model is correct, implies rising circulation velocities in the northern hemisphere and north of $-20°$ latitude. Their model for the detached haze does imply considerable enhancement of optical depths at altitudes above 250 km, compared with RP, as we require.

The planned Cassini orbiter mission will provide detailed information about Titan's atmosphere over several years centered on 2006. That time interval will be during Titan post-solstice southern hemisphere summer, and the solar aspect at Titan will therefore be approaching the one that prevailed during the Voyager encounters. As Fig. 39 shows, our high-resolution view of Titan's atmosphere during northern summer could well be the only one available during this season for many years to come,

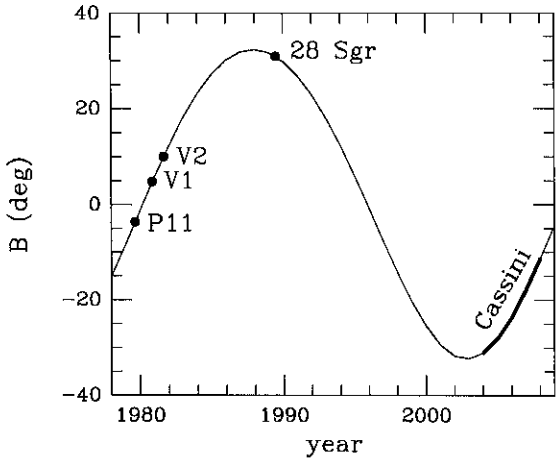

Fig. 39. Titan seasonal aspect as a function of date (B is the Titan-centered declination of the sun). The dates of spacecraft encounters by *Pioneer 11*, *Voyager 1*, and *Voyager 2* are shown, together with the planned active dates of the *Cassini* Saturn orbiter mission

and may play a significant role in constraining models for Titan's atmospheric circulation and response to solar heating.

As a careful inspection of Figs. 8 – 28 shows, our model has still not successfully reproduced every general trend in the data. In some cases our calculation of the central flash peak flux is smaller than the data, and in other cases larger. Since the detached haze in the southern hemisphere, which governs the level of the central flash, may be quite patchy as a function of altitude, it may not be possible to fit all central flashes exactly with a smooth model.

It is also evident that the observed flux falls below the model flux on the emersion side of the lightcurves at Manley, Hertford, RGO, Langwedel, and Essen (near 81800 – 81850 UT). This effect could be due to the presence of denser haze on the emersion (sunrise) side of Titan at these latitudes. Thus, a non-axially symmetric model may be needed to account for these features.

In the central flash data at Pic du Midi, a pronounced drop in the flux is seen near 81700 UT, which is not accounted for in the model. Also, at Catania, our model tends to overestimate the flux near the center of the shadow, and predicts a sharper discontinuity near the edge of the haze layer than is observed. A model which includes regional variations in haze opacity on smaller scales may be needed to fit all of the data more closely.

On still smaller scales, we see strong scintillations during the occultation at all stations. These rapid fluctuations in the stellar signal are produced by refractivity fluctuations in Titan's atmosphere (Hubbard et al. 1988b; Narayan & Hubbard 1988). Scintillations are observed throughout the height and pressure interval shown in Figs. 4 and 5, and are a major source of "noise" in the inversions for the temperature structure. We plan to conduct an analysis of the scintillations, which should lead to further information about the dynamics of Titan's high atmosphere. Our data set is well suited for this purpose.

Acknowledgements. This work has been supported by NASA grants NAGW-1555 and NAGW-596, and by NSF grant INT-8907133 (US-France cooperative research). The RGO observations were carried out using the UK Satellite Laser Ranging Facility at Herstmonceux, E. Sussex, UK, which is an outstation of the Royal Greenwich Observatory, Cambridge. We are indebted to J.L. Leroy for giving us access, on his own observing time, to the 2-m Pic du Midi Bernard Lyot Telescope for this experiment. We thank C.P. McKay for useful comments on Titan aerosols.

References

Beisker W., Bittner C., Bode H.-J., et al. 1989, Occultation Newslett. 4, 324
Coustenis A., Bézard B., Gautier D., Marten A., Samuelson R. 1991, Icarus 89, 152
Elliot J.L., French R.G., Dunham E., et al. 1977, ApJ 217, 661
Eshleman V.R. 1989, Icarus 80, 439
Flasar F.M., Conrath B.J. 1990, Icarus 85, 346
Flasar F.M., Conrath B.J., Samuelson R.E. 1981, Nat 292, 693
Forrest R.W., Nicolson I.K.M. 1990, MNRAS 243, 11P
Hansen J.E., Travis L.D. 1974, Sp. Sci. Rev. 16, 527
Hourdin F., Le Van P., Talagrand O., et al. 1992, ESA SP-338 (Proc. Symposium on Titan, Toulouse, France), 101
Hubbard W.B., Hunten D.M., Dieters S.W., Hill K.M., Watson R.D. 1988a, Nat 336, 452
Hubbard W.B., Lellouch E., Sicardy B., et al. 1988b, ApJ 325, 490.
Hubbard W.B., Yelle R.V., Lunine J.I. 1990, Icarus 84, 1 (paper HYL)
Hubbard W.B., Hunten D.M., Reitsema H.J., et al. 1990, Nat 343, 353
Hubbard W.B., Porco C.C., Hunten D.M., et al. 1992, Icarus, submitted
Hunten D.M., Tomasko M.G., Flasar F.M., et al. 1984, Titan. In: Gehrels T., Matthews M.S. (eds.) Saturn. Univ. of Arizona Press, Tucson, pp. 671-759
Khare B.N., Sagan C., Arakawa E.T., et al. 1990, Icarus 60, 127
Lellouch E., Hunten D.M., Kockarts G., Coustenis A. 1990, Icarus 83, 308
Lindal G.F., Wood G.E., Holz H.B., et al. 1983, Icarus 53, 348
McKay C.P., Pollack J.B., Courtin R. 1989, Icarus 80, 23
Narayan R., Hubbard W.B. 1988, ApJ 325, 503
Rages K., Pollack J.B. 1983, Icarus 55, 50 (paper RP)
Rages K., Pollack J.B., Smith P.H. 1983, J. Geophys. Res. 88, 8721
Sicardy B., Brahic A., Ferrari C., et al. 1990, Nat 343, 350
Smith B.A., Soderblom L., Beebe R., et al. 1981, Sci 212, 163
Smith G.R., Strobel D.F., Broadfoot A.L., et al. 1982, J. Geophys. Res. 87, A3, 1351
Tassoul J.-L., 1978, Theory of Rotating Stars. Princeton University Press, Princeton, N.J., USA
Tomasko M.G., Smith P.H. 1982, Icarus 51, 65
Toon O.B., McKay C.P., Griffith C.A., Turco R.P. 1992, Icarus 95, 24
Washburn E.W., 1930, International Critical Tables of Numerical Data – Physics, Chemistry and Technology, vol. 7. McGraw-Hill, New York, p. 11
West R.A., Smith P.H. 1991, Icarus 90, 330
Yelle R.V. 1991, ApJ 383, 380

This article was processed by the author using Springer-Verlag TEX A&A macro package 1992.